Plasma Assisted Combustion and Chemical Processing

Yiguang Ju and Andrey Starikovskiy

First published 2025

ISBN: 9781032066103 (hbk)
ISBN: 9781003203063 (ebk)

Chapter 5
Plasma-Assisted Combustion Chemistry

DOI: 10.1201/9781003203063-5

CRC Press
Taylor & Francis Group
Boca Raton London New York

CRC Press is an imprint of the
Taylor & Francis Group, an **informa** business

5 Plasma-Assisted Combustion *Chemistry*

5.1 ELEMENTARY REACTIONS IN COMBUSTION

5.1.1 Chain-Initiation, Propagation, and Termination Reactions in Combustion

Fuel oxidation and heat release in the combustion process are proceeded through radical production, multiplication, and recombination. As such, radicals such as H, O, OH, CH_3, and HO_2 play the most critical role in combustion. There are several key reaction processes that govern radical production and consumption. They are, respectively, the chain-initiation, branching, propagation, and termination reactions (Table 5.1).

Chain-initiation reaction: As shown in Table 5.1, the chain-initiation reaction is a reaction that reactants produce one or more radicals in the molecule collision processes. This reaction is very important in initiating the ignition and reaction processes because it produces the first group of radicals directly from reactants. However, as shown in Figure 5.1, the chain-initiation reactions typically have a very high activation energy ($E_{a,i}$) because the reactants (A and B) are stable molecules in the ground states. Therefore, this type of reaction is very slow and can be rate limiting in an ignition process. However, as shown later, plasma can provide new reaction pathways at low temperature via electrons and excited species to produce radicals rapidly by bypassing the rate-limiting slow chain-initiation reactions in combustion.

Chain-branching reaction: The chain-branching reaction is a reaction that one radical reacts with a reactant and produces two or more radicals. This reaction is like the nuclear fission reactions that magnify the radical pool to accelerate the reaction processes. However, the chain-branching reactions also have quite high activation energies ($E_{a,b}$), although they may be lower than that of the chain-initiation reactions. Therefore, the chain-branching reactions are the most important rate-limiting reactions (after initial radicals are produced) that dominate the rate of reaction processes and the burning rate of combustion. As such, understanding the key chain-branching reactions and knowing how to control them using plasma is critical in plasma-assisted combustion.

Chain-propagation reaction: The chain-propagation reaction is a reaction that one radical (e.g., H) reacts with another reactant and produces another radical (e.g., OH) in the combustion processes. Although this reaction is less important than the chain-branching reactions in affecting the rate of radical pool growth, it normally has lower activation energy and thus can strongly affect fuel oxidation, intermediate species production, and heat release rate.

TABLE 5.1
Schematic of Chain-Initiation, Branching, Propagation, and Termination Reactions, *A* and *B* Are the Reactants, *R* the Radicals, and *P* the Product, Respectively

$A + B = 2R$	Initiation
$A + R = 2R$	Branching
$A + R = R + P$	Propagation
$R + R = 2P + \text{heat}$	Termination

DOI: 10.1201/9781003203063-5

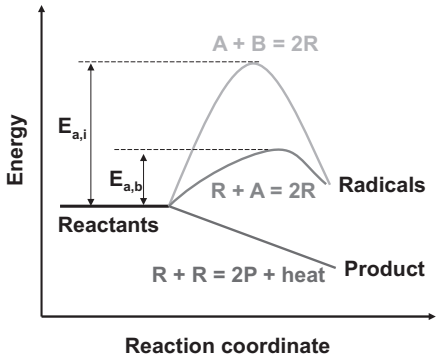

FIGURE 5.1 Schematic of activation energies and enthalpy changes of chain-initiation, branching, and termination reactions.

Chain-termination reaction: The chain-termination reaction is a reaction that two radicals react together or with a third molecule and produce a stable product with one or two less active radicals. Therefore, in this process, the radial number will decrease, and the reaction will slow down. Sometimes, we refer to it as radical quenching reaction. However, the chain-termination reaction is important to shift the chemical equilibrium toward the products and produce heat to raise the temperature to self-accelerate the reaction process.

Reaction rate and the Arrhenius law: For reaction to occur, as shown in Figure 5.1, the energy of the colliding reactants needs to be greater than or equal to the activation energy (E_a). The kinetic energy of a molecule is proportional to temperature. However, not every molecule has the same amount of energy. In equilibrium, the energy of molecules follows the Boltzmann distribution (Figure 1.25), that is, the number of molecules with energy, E, is proportional to exp ($-E/R_0T$). Thus, only a very small portion of the molecules have enough energy to induce a reaction after a collision. From statistical mechanics, by using the activation energy as the reaction threshold and the Boltzmann energy distribution, one can derive the *Arrhenius law* for the reaction rate, k, as a function of temperature, T, and the activation energy, E_a, as,

$$k = AT^n e^{-E_a/R_0T} \tag{5.1}$$

where A is the pre-exponential factor, R_0 is the universal gas constant, and n is a constant, respectively. Therefore, to accelerate the reaction rate, one needs to reduce the activation energy by creating a new reaction pathway or raising the temperature.

5.1.2 Elementary Kinetics of Hydrogen

Hydrogen is a green and the simplest fuel. Moreover, the hydrogen combustion mechanism is the base mechanism for all combustion mechanisms of other fuels. Therefore, it is critical to understand the key chain-initiation, branching, propagation, and termination reactions in hydrogen combustion. A detailed hydrogen mechanism recently updated for high-pressure combustion [1] (HP-Mech) is shown in Table 5.2.

In the hydrogen reaction system, the major chain-initiation, branching, propagation, and termination reactions are as follows:

Chain-initiation reactions:

$$H_2 + O_2 = H + HO_2 \tag{R5.1a}$$

$$H_2 + O_2 = OH + OH \tag{R5.2}$$

TABLE 5.2
Detailed Reaction Kinetics of Hydrogen Combustion in HP-Mech [1]

Reactions	*A* ($cm^3/(mol \cdot s \cdot K)$)	*n*	E_a (cal/mol)
$H + O_2 = O + OH$	7.26E+14	–0.235	15928.7
$OH + OH = O + H_2O$	9.32E+03	2.564	–2603.7
$H + H + H_2 = H_2 + H_2$	1.02E+17	–0.6	0
$H + OH(+M) = H_2O(+M)$	2.51E+13	0.234	–114
LOW	4.50E+25	–3.064	1581.4
TROE	0.72	1.0E-30	1.0E+30
$H + O_2(+M) = HO_2(+M)$	1.03E+12	0.604	–241.1
LOW	1.74E+19	–1.23	0
TROE	0.495	1.0E–30	1.0E+30
$HO_2 + OH = O_2 + H_2O$	7.44E+12	0.055	–915.2
DUP	1.17E+23	–2.156	23,681
$HO_2 + HO_2 = H_2O_2 + O_2$	1.93E-02	4.12	–4,960
$HO_2 + HO_2 = OH + OH + O_2$	6.41E+17	–1.54	8,540
$H_2O_2 + H = H_2 + HO_2$	4.40E+01	3.45	712
$H_2O_2 + H = H_2O + OH$	3.35E+07	1.91	3,654
$H_2O_2(+M) = 2OH(+M)$	2.00E+12	0.9	48,749
LOW	2.49E+24	–2.3	48,749
TROE	0.43	1.0E–30	1.0E+30

LOW and TROE indicate the low- and high-pressure rate limiting, respectively; DUP indicates the reaction rate constant equals to the summation of those identical reactions; M indicates a third body.

Chain-branching reactions:

$$H + O_2 = OH + O \quad \text{(R5.3)}$$

$$O + H_2 = OH + H \quad \text{(R5.4)}$$

$$H_2O_2 = OH + OH \quad \text{(R5.5)}$$

Chain-propagation reactions:

$$OH + H_2 = H_2O + H \quad \text{(R5.6)}$$

$$HO_2 + H = OH + OH \quad \text{(R5.7)}$$

Chain-termination reactions:

$$H + O_2(+M) = HO_2(+M) \quad \text{(R5.8)}$$

$$H + OH(+M) = H_2O(+M) \quad \text{(R5.9)}$$

$$HO_2 + H = H_2 + O_2 \quad \text{(R5.1b)}$$

$$HO_2 + OH = H_2O + O_2 \quad \text{(R5.10)}$$

$$HO_2 + HO_2 = H_2O_2 + O_2 \quad \text{(R5.11)}$$

As discussed before, since the slowest chain-branching reaction (R5.3) is the rate-limiting reaction, from Figure 5.2 we can see that if there is one H radical in the reaction system, reaction R5.3 will produce one OH and one O. Since R5.6 is a very fast reaction, the OH produced from R5.3 will be immediately converted to a new H by R5.6. Then, because R5.4 is also faster than R5.3, the O produced in R5.3 will be converted to the second H and a new OH from R5.4. The resulting new OH will be converted to the third H via the fastest reaction R5.6 again. As a result, by adding up reactions R5.3 and R5.4 with twice of reaction R5.6, as seen in Figure 5.2, one H radial will produce 3H radicals in the hydrogen chain-branching and propagation system. Therefore, the slowest chain-branching reaction R5.3 is a dominant chain-branching reaction for H radical production at high temperature, especially in flames and high-temperature ignition (HTI):

High-temperature chain-branching reaction:

$$H + O_2 = OH + O \quad \text{(R5.3)}$$

Note that the H radical for the chain-branching reaction R5.3 can be suppressed via the following chain-termination reaction,

Chain-termination reaction:

$$H + O_2(+M) = HO_2(+M) \quad \text{(R5.8)}$$

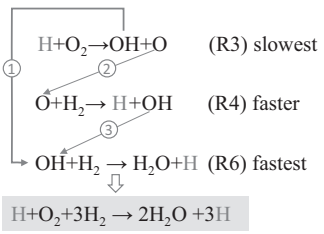

FIGURE 5.2 One H radical produces three H radicals via the slowest rate-limiting reaction of R5.3 and the faster reactions of R5.4 and R5.6 (R_3, R_4, and R_6 in this figure are referred to as R5.3, R5.4, and R5.6).

Figure 5.3 shows the comparison of the reaction rates between the chain-branching reaction R5.3 and the termination reaction R5.8 at different pressures with air, H_2O, and CO_2 as the third body (M), respectively. It is seen clearly that with the decrease of temperature, the termination reaction R5.8 is faster than the branching reaction R5.3. With the increase of pressure, the balance of these two competing reactions shift to higher temperature. At 25 atm, a typical gas turbine pressure, the temperature at which the two reaction rates become equal increases to 1,250 K. Moreover, if H_2O and CO_2 are used as the diluents, the increased third-body effect makes the termination reaction even faster and further raises the critical reaction temperature.

Therefore, the competition between the chain-branching reaction R5.3 and chain-termination reaction R5.8 will determine the combustion limits and is strongly pressure and diluent-dependent.

The hydrogen explosion limits:

Since reactions R5.4 and R5.6 are fast (Figure 5.2), the consumption rates of O and OH are faster than their production rates via R5.3. Therefore, the concentration of these two radicals (OH and O) will be in *quasi-steady state*, i.e., their net production rates are almost zero. With this assumption, the radical production via reactions R5.3, R5.4, R5.6, and R5.8 can be written as

$$\frac{dC_{\mathrm{H}}}{dt} = -k_3 C_{\mathrm{H}} C_{\mathrm{O}_2} - k_8 C_{\mathrm{H}} C_{\mathrm{O}_2} C_{\mathrm{M}} - k_4 C_{\mathrm{O}} C_{\mathrm{H}_2} - k_6 C_{\mathrm{OH}} C_{\mathrm{H}_2} \tag{5.2a}$$

$$\frac{dC_{\mathrm{OH}}}{dt} = k_3 C_{\mathrm{H}} C_{\mathrm{O}_2} + k_4 C_{\mathrm{O}} C_{\mathrm{H}_2} - k_6 C_{\mathrm{OH}} C_{\mathrm{H}_2} \simeq 0 \tag{5.2b}$$

$$\frac{dC_{\mathrm{O}}}{dt} = k_3 C_{\mathrm{H}} C_{\mathrm{O}_2} - k_4 C_{\mathrm{O}} C_{\mathrm{H}_2} \simeq 0 \tag{5.2c}$$

By submitting the OH and O concentrations from Eqs. 5.2b and 5.2c into Eq. 5.2a, we will have

$$\frac{dC_{\mathrm{H}}}{C_{\mathrm{H}}} = \left(2k_3 - k_8 C_{\mathrm{M}}\right) C_{\mathrm{O}_2} dt \tag{5.3}$$

The above equation indicates that there is a critical limit that define whether the hydrogen reaction system is explosive or non-explosive,

$$\frac{2k_3}{k_8 C_{\mathrm{M}}} \begin{cases} > 1, & \text{explosive} \\ < 1, & \text{non-explosive} \end{cases} \tag{5.4}$$

This is the so-called *the second explosion limit* (Figure 5.4) [2], which is a result of the competition between the chain-branching and termination reactions, R5.3 and R5.8. The second explosion limit occurs at intermediate pressures and increases with the increase of temperature.

At low pressure, the reaction rate of R5.8 is very slow and negligible. As a result, the radical quenching is mainly via H radical diffusion and quenching on the wall. Therefore, the first explosion limit at low pressure (Figure 5.4) is governed by R5.3 and radical loss due to diffusion and increases with the decrease of temperature.

At high pressure, HO_2 radical production via R5.8 becomes more important (Figure 5.3). With the increase of HO_2 concentration, the reactions R5.5 and R5.7 become the new chain-branching reactions at high pressure. Therefore, the HO_2 chemistry leads to the third explosion limit at high pressure, which increases again with the decrease of the temperature (Figure 5.4). A sensitivity analysis of the burning rate of a hydrogen flame on the rates of elementary reactions is shown in Figure 5.5. It clearly shows the increased sensitivity of reaction R5.8 and R5.3 at high pressure.

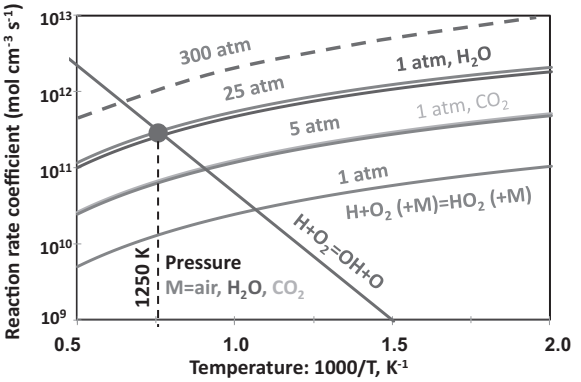

FIGURE 5.3 Reaction rate comparison between $H+O_2=OH+O$ and $H+O_2(+M)=HO_2(+M)$ at different pressures and with air, H_2O, and CO_2 as the diluents, respectively.

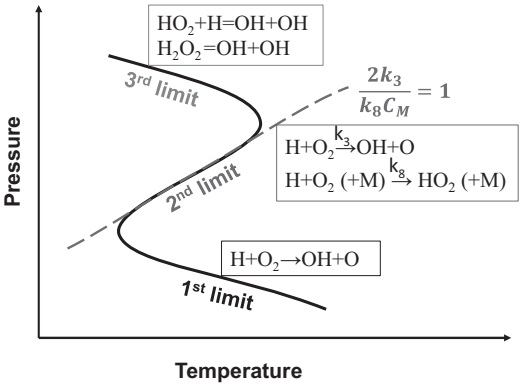

FIGURE 5.4 Schematic of the hydrogen explosion limits and the key reactions. The region on the right of the explosion limit curve is the explosive region (k_3 and k_8 are referred to as R5.3 and R5.8).

If the system temperature is further reduced (Figure 5.3), the H radical production via reaction R5.3 will be very slow and negligible. Therefore, the major chain-branching reaction at intermediate temperature (700–1,100 K) and high pressure will be:

Intermediate-temperature chain-branching reaction:

$$H_2O_2 \rightarrow OH + OH \tag{R5.5}$$

Therefore, the two chain-branching reactions of R5.3 and R5.5 play a dominant role in hydrogen combustion chemistry for H and HO_2 radical production at high and intermediate temperatures, respectively.

5.1.3 Elementary Kinetics of Methane

Methane is an important fuel for power, heating, carbon, and hydrogen production. Oxidation of methane at fuel lean conditions is very important to reduce emissions and methane slip. Unfortunately, unlike hydrogen, methane is much more difficult to oxidize than hydrogen because of the strong C–H bond in methane (~439 kJ/mole) and CH_3 (~463 kJ/mol) [3], resulting in slow CH_4 chain-initiation and branching channels.

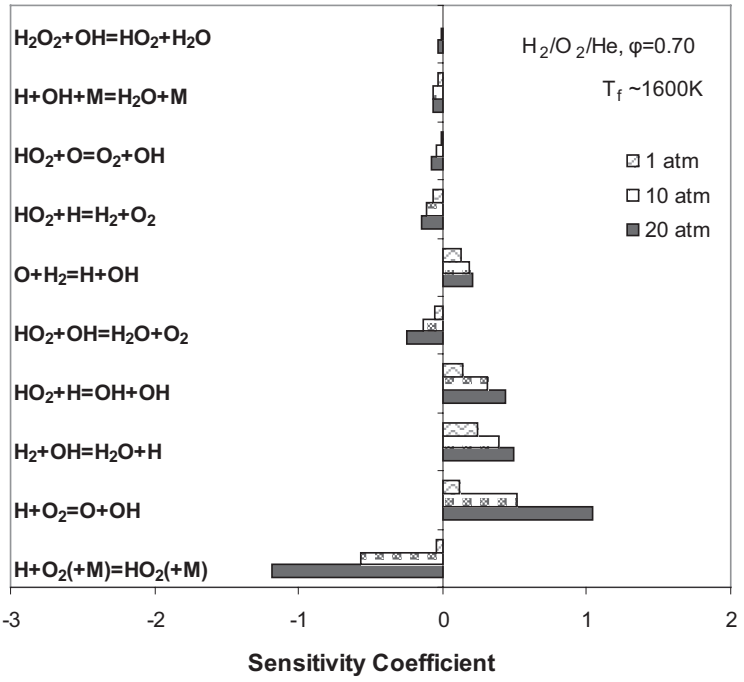

FIGURE 5.5 Reaction sensitivity of lean hydrogen combustion ($\varphi = 0.7$) at 1, 10, and 20 atm, respectively.

The major chain-initiation, branching, propagation, and termination reactions of methane at high temperature are listed below. The first radical production in chain-initiation reaction is via R5.12. After this initiation reaction, CH_3 will be oxidized via chain-branching and propagation reactions R5.14 and R5.15 to form CH_3O as well as O or OH radicals. However, these reactions are slower than R5.3. Therefore, methane oxidation is slower than that of hydrogen. To proceed methane oxidation, it is critical to produce H radials to accelerate R5.3 branching reaction. CH_3O radicals will be converted to CH_2O and HCO via reactions R5.16 and R5.17, respectively. The H-abstraction reaction by radicals from CH_2O in reaction R5.17 is one of the major exothermic reactions in methane oxidation. In methane oxidation, reaction R5.18a is a critical reaction to produce H radicals for R5.3. However, R5.18b is a termination reaction to produce relatively inactive HO_2. Note that different from R5.8 in hydrogen mechanism, R5.18b is the major reaction of HO_2 production in methane oxidation. Therefore, like R5.3 and R5.8 for hydrogen, reactions R5.18a and R5.18b are the major competition reaction pairs for methane oxidation (Figure 5.6). As such, producing H and OH radicals by plasma can dramatically accelerate methane oxidation via R5.3. Depending on the temperature, CO will be oxidized to CO_2 and produce heat via reactions R5.19 and R5.20, respectively, at high and intermediate temperatures. Note that at high pressure, the pressure fall-off reaction R5.13 and the termination reactions R5.8 and R5.21 will play important roles in affecting methane oxidation.

Chain-initiation reactions:

$$CH_4 + O_2 = CH_3 + HO_2 \tag{R5.12}$$

$$CH_4(+M) = CH_3 + H(+M) \tag{R5.13}$$

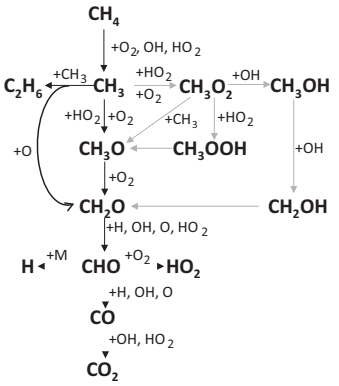

FIGURE 5.6 Schematic of methane oxidation at high (black arrow) and low (green arrow) temperatures, respectively. The dashed box indicates H radical production and termination competition reaction pare.

Chain-branching reactions:

$$H + O_2 = OH + O \tag{R5.3}$$

$$CH_3 + O_2 = CH_3O + O \tag{R5.14a}$$

Chain-propagation reactions:

$$CH_3 + O_2 = CH_2O + OH \tag{R5.14b}$$

$$CH_3 + HO_2 = CH_3O + OH \tag{R5.15}$$

$$CH_3O + O_2 = CH_2O + HO_2 \tag{R5.16}$$

$$CH_2O + X = HCO + XH\left(X = H, OH, O, HO_2\right) \quad \text{Exothermic} \tag{R5.17}$$

$$HCO(+M) = CO + H(+M) \tag{R5.18a}$$

$$HCO + O_2 = HO_2 + CO \tag{R5.18b}$$

$$CO + HO_2 = CO_2 + OH \tag{R5.19}$$

$$CO + OH = CO_2 + H \quad \text{Exothermic} \tag{R5.20}$$

Chain-termination reactions:

$$H + O_2(+M) = HO_2(+M) \tag{R5.8}$$

$$CH_3 + CH_3(+M) = C_2H_6(+M) \tag{R5.21}$$

To summarize the discussions above, a schematic of the reaction pathways of methane oxidation at high and low temperatures is shown in Figure 5.6. Note that at low temperature and high pressure, production of methyldioxy radical, CH_3O_2, from CH_3 with O_2 and HO_2 becomes important. Therefore, new low-temperature reaction channels via $CH_3 \rightarrow CH_3O_2 \rightarrow CH_3O$ pathway and $CH_3 \rightarrow CH_3O_2 \rightarrow CH_3OOH \rightarrow CH_2O$ pathway will become important at low temperature and high pressure [4]. Understanding the rate-limiting reactions, the competing radical production reaction pairs, and the low and high-temperature/-pressure reaction pathways are important for plasma-assisted combustion. Since nonequilibrium plasma operates at low temperature, the low-temperature methane oxidation via CH_3O_2 will be accelerated.

5.1.4 Reaction Kinetics of Ammonia

Ammonia is likely to be an important hydrogen carrier for power generation and energy storage. However, ammonia is difficult to ignite and has a very low flame speed and high NO_x formation in combustion [5–7]. Therefore, it is necessary to understand ammonia combustion chemistry and to explore the possibility of plasma-enhanced ammonia combustion.

Ammonia combustion chemistry has been studied extensively since the 1980s [8,9]. To improve the burning properties of ammonia, more interest in ammonia combustion is to understand the combustion kinetics of ammonia in blended fuel mixtures with hydrogen, methane, large alkanes, and oxygenated fuels. Figure 5.7 shows a summary of the recent studies of ammonia combustion kinetics with hydrogen, alkanes, alcohols, and ethers. It is seen that most of the kinetic studies were conducted in high-temperature flames under low pressure (0.3–10 atm) [10–32] with hydrogen and hydrocarbon blends [6,7,33–50]. However, kinetic studies of ammonia oxidation with oxygenated fuels [51–61] are very scarce and many studies have been limited to low pressures. To data, only

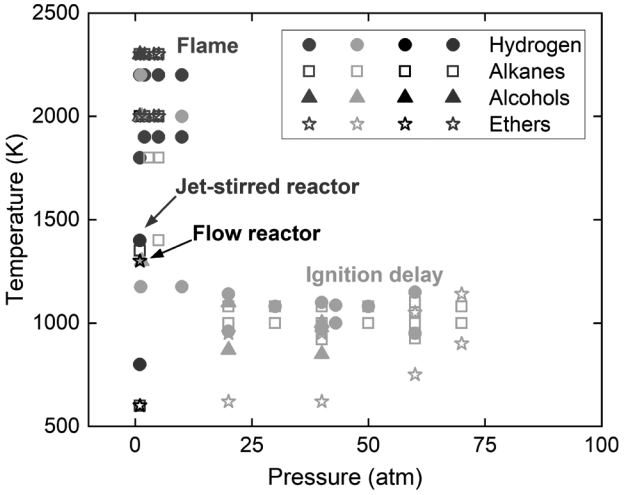

FIGURE 5.7 Pressure and temperature conditions of kinetic studies of NH_3 oxidation with different fuel blends.

the ignition delay time of ammonia with H_2, alcohols, and ethers are studied up to 70 atm [53–55,58,59,61] using a rapid compression machine (RCM) or shock tube [35]. To overcome this pressure limitation, Hashemi et al. [62,63] succeeded in species measurements at 100 atm for $CH_4/C_2H_6/C_3H_8/C_7H_{16}/NH_3$ oxidations [6,35,62–64]. Glarborg and Ju [35] also collaborated in extending these studies for high-pressure alkane/NH_3 oxidation using a new supercritical pressure jet-stirred reactor (SP-JSR), which can operate up to 250 atm with a well-defined temperature (±5 K) and engine relevant flow residence time (50–500 ms) [1,4,65–67]. The results showed a strong kinetic coupling between n-heptane and ammonia oxidation at low and intermediate temperature at high pressure.

The major chain-initiation, branching, propagation, and termination reactions of ammonia combustion are as follows [5,8,9,68,69],

Chain-initiation reactions:

$$NH_3(+M) = NH_2 + H(+M) \tag{R5.22}$$

$$NH_3 + O_2 = NH_2 + HO_2 \tag{R5.23}$$

Chain-branching reactions:

$$H + O_2 = OH + O \tag{R5.3}$$

$$NH_2 + NO = NNH + OH \tag{R5.24a}$$

Chain-propagation reactions:

$$NH_2 + O_2 = HNO + OH \tag{R5.25}$$

$$NH + O_2 = HNO + O \tag{R5.26}$$

$$NH_3 + X = NH_2 + XH\left(X = H, O, OH, HO_2\right) \tag{R5.27}$$

$$NH_2 + X = NH + XH\left(X = H, O, OH\right) \tag{R5.28}$$

$$NH_2 + O = HNO + H \tag{R5.29}$$

$$HNO(+M) = NO + H(+M) \tag{R5.30}$$

$$HNO + O_2 = HO_2 + NO \tag{R5.31}$$

$$NH + NO = N_2O + H \quad \text{(R5.32a)}$$

$$NH + NO = N_2 + OH \quad \text{(R5.32b)}$$

$$NH + OH = HNO + H \quad \text{(R5.33)}$$

$$NH + X = N + XH(X = H,O,OH) \quad \text{(R5.34)}$$

$$NH + O = NO + H \quad \text{(R5.35)}$$

$$N_2O + H = N_2 + OH \quad \text{(R5.36)}$$

$$N + NO = N_2 + O \quad \text{(R5.37)}$$

$$N + O_2 = NO + O \quad \text{(R5.38)}$$

$$NH_2 + HO_2 = H_2NO + OH \quad \text{(R5.39a)}$$

$$H_2NO + HO_2 = HNO + H_2O_2 \quad \text{(R5.40)}$$

$$NO + HO_2 = NO_2 + OH \quad \text{(R5.41)}$$

$$NH_2 + NO_2 = H_2NO + NO \quad \text{(R5.42a)}$$

Chain-termination reactions:

$$NH_2 + HO_2 = NH_3 + O_2 \quad \text{(R5.39b)}$$

$$NH_2 + HO_2 = HNO + H_2O \quad \text{(R5.39c)}$$

$$NH_2 + NO_2 = N_2O + H_2O \quad \text{(R5.42b)}$$

$$NH_2 + HNO = NH_3 + NO \quad \text{(R5.43)}$$

$$NH_2 + NO = N_2 + H_2O \quad \text{(R5.24b)}$$

$$NH_2 + NH_2(+M) = N_2H_4(+M) \quad \text{(R5.44)}$$

$$HNO + OH = NO + H_2O \quad \text{(R5.45)}$$

$$N + OH = NO + H \quad \text{(R5.46)}$$

$$H + O_2(+M) = HO_2(+M) \quad \text{(R5.8)}$$

The main chain-initiation reaction is reaction R5.23 which is very slow because of the strong N–H bond of NH_3. At high temperature, the ammonia oxidation is schematically shown in Figure 5.8a [9]. Equation R5.3 remains to be the key chain-branching reaction to produce H/O/OH radicals. NH_3 is then mainly consumed by H-abstraction reactions via R5.27 and R5.28 and from NH_2 and NH. Both of them are further oxidized by O, OH, and O_2 via reactions R5.24, R5.26, R5.29, R5.33, and R5.35 to form HNO and NO. NH can be further reduced to N with O and H radicals via reaction R5.34. In addition, NH_2 and NH reactions with NO will lead to NNH and N_2O via reactions R5.24a and R5.32b. Then, NO reactions with NH_2 and N can lead to NO reduction to N_2 from R5.24b and R5.37.

At lower temeprature and high pressure, due to the importance of HO_2 chemistry (R5.8), R5.39b and R5.39c start to compete with R5.39a for radical progagation and termination. Reactions R5.39–R5.42 will further couple NO, NO_2, and H_2NO production and consumption by HO_2, leading to a complicated coupling between NH_3 oxidation, HO_2 chemistry, H_2NO reactions, and NO_x chemistry at lower temperatures (Figure 5.8b). Unfortunately, this kinetic coupling at high pressure is not well understood.

Figure 5.9a shows the energy barriers of reactions R5.39, $NH_2 + HO_2$ [69]. It is seen that the termination reaction R5.39b has the lowest energy barrier. Therefore, NH_3 oxidation at high pressure is very sensitive to the branching ratios of reaction R5.39. Unfortunately, although quantum chemistry calculations have been done for this reaction [69], few experimental measurements of this reaction have been conducted because of the difficulty in quantifying radial-radical reactions involving HO_2. With the introduction of oxygenated fuels and low-temperature plasma, more HO_2 will be formed and this reaction coupling will become even more important. As shown in the ammonia oxidation

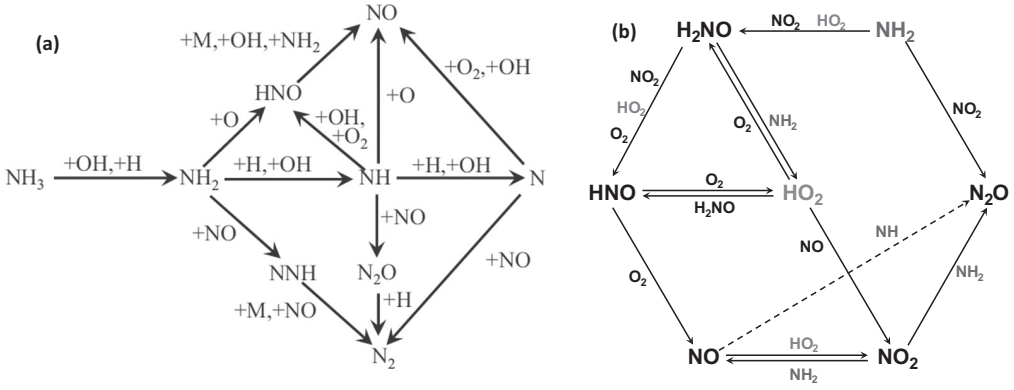

FIGURE 5.8 (a) Schematic of high-temperature NH_3 oxidation kinetics [9]. (b) Schematic of low-temperature and high-pressure kinetic coupling between HO_2 chemistry, ammonia oxidation, and NO_x chemistry.

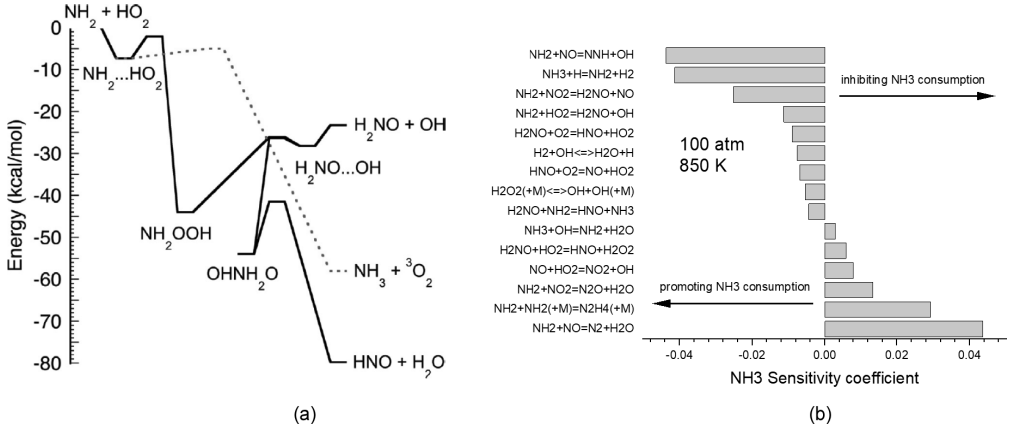

FIGURE 5.9 (a) Energy barriers of NH_2+HO_2 [69] reaction pathways. (b) Reaction sensitivity analysis of NH_3 concentration at 100 atm, 850 K, and fuel lean conditions.

sensitivity analysis of elementary reactions at high pressure and low temperature (Figure 5.9b), there is a strong kinetic coupling between ammonia oxidation via NH_x+HO_2 chemistry, NH_x+NO_x reaction channels, and NO_x chemistry as well as RO_2+NO and HO_2+NO reaction pathways [69–71].

5.1.5 Reaction Kinetics of Large Alkanes and Oxygenates at Different Temperatures

For large hydrocarbon fuels such as n-alkanes and oxygenated fuels such as alcohols [72,73], ethers [66,67,74,75], and esters [76,77], in addition to the low and intermediate temperature chain-branching reactions R5.48 and R5.50 (Table 5.3), there exist low-temperature chain-branching reactions via alkyl-peroxy radicals, which results in low-temperature chemistry (LTC) and cool flames below 900 K [78,79] (Figure 5.10). As shown in Figure 5.10, for a large alkane or oxygenate fuel, in addition to the HTI above 1,000 K, there exists a low-temperature ignition (LTI) between 500 and 900 K due to LTC. Corresponding to the LTI, there exists a cool flame at a temperature far below the hot flame (typically above the critical chain-branching temperature of R5.48 around 1,100 K). The existence of LTI and cool flame significantly changes the ignition delay time and the flammability limit of the combustion process and provides a great opportunity for nonequilibrium plasma to control low-temperature combustion [78,79].

Figure 5.11a shows the dependence of the ignition delay time on the initial temperature for a stoichiometric n-heptane/air mixture at 20 atm with and without 100 ppm OH addition (e.g., generated by plasma). The solid and dashed lines, respectively, represent the ignition delay times of HTI and LTI. It is clearly seen that radical addition by plasma in the initial mixture can dramatically reduce the ignition delay time of LTI to 100 μs. Thus, through chemical sensitization by plasma, LTI can be accelerated dramatically.

The schematic of temperature-dependent chain-branching reaction pathways for fuel oxidation is shown in Figure 5.12 [79–83] and the key elementary reactions for low and intermediate temperature are shown in Table 5.3. At a low temperature (below 700 K), LTC chain-branching pathway governs the rate of fuel oxidation. As shown in Figure 5.12, at LTC, fuel (RH) oxidation starts with an H-abstraction of fuel by radicals such as OH/HO_2 and forms a fuel radical (R). Then, the fuel radicals (R) are added by an O_2 molecule to form RO_2 or HO_2. The internal isomerization of RO_2 will lead to QOOH (hydrocarbon hydrogen peroxide). The subsequent oxygen addition to QOOH for O_2QOOH and its beta scissions produce multiple OH radicals (Figure 5.12). This LTC results in the first stage LTI and cool flame as shown in Figure 5.10. As such, the major cool flame chain-branching reaction pathway can be written as:

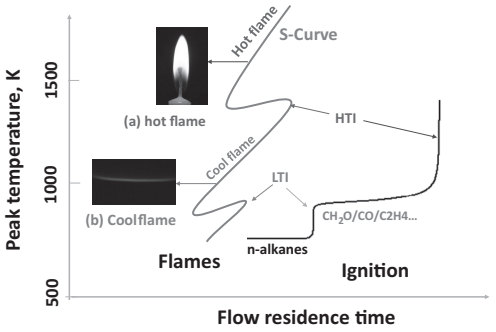

FIGURE 5.10 Schematic of the dependence of peak temperature for low-temperature ignition (LTI), high-temperature ignition (HTI), cool flame, and hot flame on flow residence time for a large n-alkane.

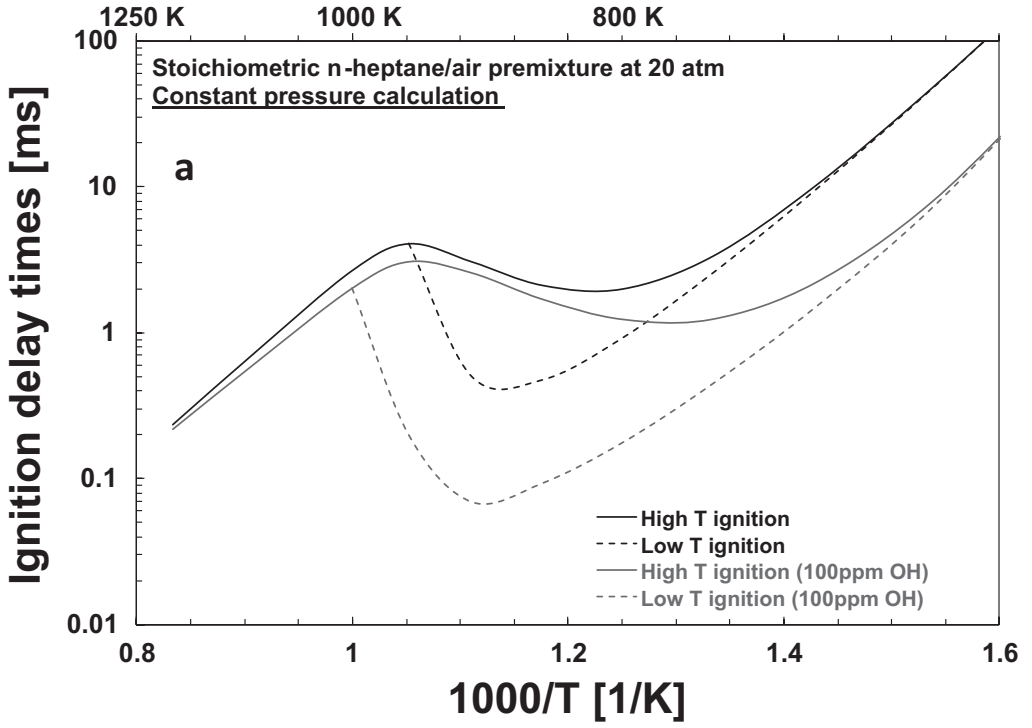

FIGURE 5.11 Dependence of the ignition delay time on the initial temperature for a stoichiometric *n*-heptane/air mixture at 20 atm with and without 100 ppm OH addition by plasma.

$$R \rightarrow RO_2 \rightarrow QOOH \rightarrow O_2QOOH \rightarrow OQ'O + 2OH \quad \text{(R5.56)}$$

At an intermediate temperature (700–1,050 K), as shown in Figure 5.12 and Table 5.3, the decompositions of RO_2, QOOH and O_2QOOH via $RO_2 \rightarrow R + O_2$ (R5.48), QOOH$\rightarrow HO_2$ + alkene or OH + cyclic ether (R5.50), and O_2QOOH $\rightarrow$ QOOH+O_2 (R5.51) shut down the O_2QOOH chain-branching pathway and slow down the reactivity, leading to the negative temperature coefficient (NTC) effect [81,84,85]. As a result, in this NTC process, the concentrations of HO_2 and fuel radicals R increase. Therefore, HO_2 reactions with fuel radicals (R5.52) and partially oxidized intermediate species (R5.47 and R5.55) as well as the H_2O_2 decomposition reaction (R5.5) become critical to produce

TABLE 5.3
Low- and Intermediate-Temperature Chemistry

$Fuel + HO_2 = R + H_2O_2$	(R5.46)
$Aldehyde + HO_2 = H_2O_2 + RCO$	(R5.47)
$RO_2 = R + O_2$	(R5.48)
$RO_2 \rightarrow QOOH$	(R5.49a)
$RO_2 \rightarrow aldehyde + HO_2$	(R5.49b)
$QOOH \rightarrow cyclic\ ether + OH$	(R5.50a)
$QOOH \rightarrow alkene + HO_2$	(R5.50b)
$O_2QOOH \rightarrow QOOH + O_2$	(R5.51)
$R + HO_2 = RO + OH$	(R5.52)
$RO + O_2 = aldehyde + HO_2$	(R5.53)
$RCO + O_2 = aldehyde + CO + OH$	(R5.54)
$HO_2 + CH_2O = H_2O_2 + HCO$	(R5.55)
$HO_2 + HO_2 = H_2O_2 + O_2$	(R5.11)
$H_2O_2 = 2OH$	(R5.5)

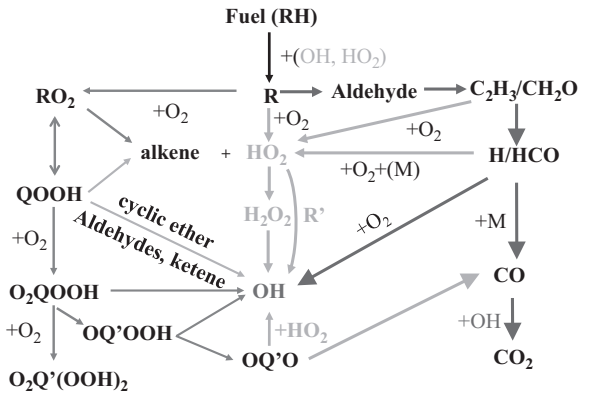

FIGURE 5.12 A schematic of the key reaction pathways at different temperatures (blue arrow: below 700 K; green arrow: 700–1,050 K; red: above 1,050 K).

OH radicals for chain-branching. Therefore, at the intermediate temperature, the HO_2 chemistry listed in Table 5.3 is the major chain-branching pathway for the second stage ITI (Figure 5.11) and warm flame formation [70,86–88]. At high pressure, recent studies have shown that HO_2 chemistry plays a critical role in fuel oxidation and the NTC effects [63,89]. As such, the major chain-branching reaction pathway for ITI and warm flame can be written as Ref. [79],

$$R' + HO_2 \rightarrow R'O + OH,\ CH_2O \rightarrow HCO \rightarrow HO_2 \rightarrow H_2O_2 \rightarrow 2OH \quad \text{(R5.57a)}$$

$$R'CO + O_2 \rightarrow aldehyde + CO + OH,\ CH_2O \rightarrow HCO \rightarrow HO_2 \rightarrow H_2O_2 \rightarrow 2OH \quad \text{(R5.57b)}$$

The above three sets of chain-branching reaction pathways in reactions R5.56, R5.57, and R5.3, respectively, represent the dominant radical production reactions at low, intermediate, and high temperatures. As will be discussed in the sections below, these three sets of temperature-dependent chain-branching reactions lead to three different kinds of flames: cool flame, warm flame, and hot flame.

5.2 CHEMICAL KINETICS IN PLASMA-ASSISTED COMBUSTION

5.2.1 Nonequilibrium Plasma Energy Transfer and Its Impact on Combustion

As discussed in Chapters 3 and 4, plasma is a nonequilibrium energy transfer process. The heat, radicals, ions, and excited species produced in plasma will affect combustion chemistry and transport. Figure 5.13 schematically shows the nonequilibrium energy transfer processes as well as active species and fast and slow heating production in plasma. When an electron gains energy in an electric field, it will collide with neutral molecules and produce a second electron and a positive ion. When electrons and positive ions recombine, it will generate heat and emit photons. Both energetic electrons and photons will create ionization, excitation, and dissociations of neutral molecules and lead to the formation of ions, excited molecules, and radicals. This process occurs within a few nanoseconds. As shown in Figure 5.13, in addition to electrons, the resulting electronically excited molecules will also collide with neutral molecules to produce vibrational molecule excitations, radicals, and fast heating from nanoseconds to microseconds. After that molecules at higher vibrational energy states will be relaxed to lower states via vibrational-vibrational (V-V) and vibrational-translational (V-T) energy transfer and generate slow heating. This process occurs from a few microseconds to milliseconds depending on the excited molecules and pressure. If the rate of V-T energy transfer is faster than that of molecule excitation by electrons and photons, the plasma will be relaxed to equilibrium plasma. Otherwise, the plasma will be in nonequilibrium and the electron and vibrational energies are much higher than the rotational and translational energies of the neutral molecules. Therefore, plasma-assisted combustion is strongly affected by the active species production in plasma.

In fact, the active species production and nonequilibrium energy transfer in plasma are a function of electron energy distribution function (EEDF) or the reduced electric field (E/N). Figure 5.14 shows the energy transfer fractions from electrons to different energy states as a function of the reduced electric field for a CH_4/H_2/He mixture. It is seen that when the E/N is below 50 Td, plasma delivers most energy

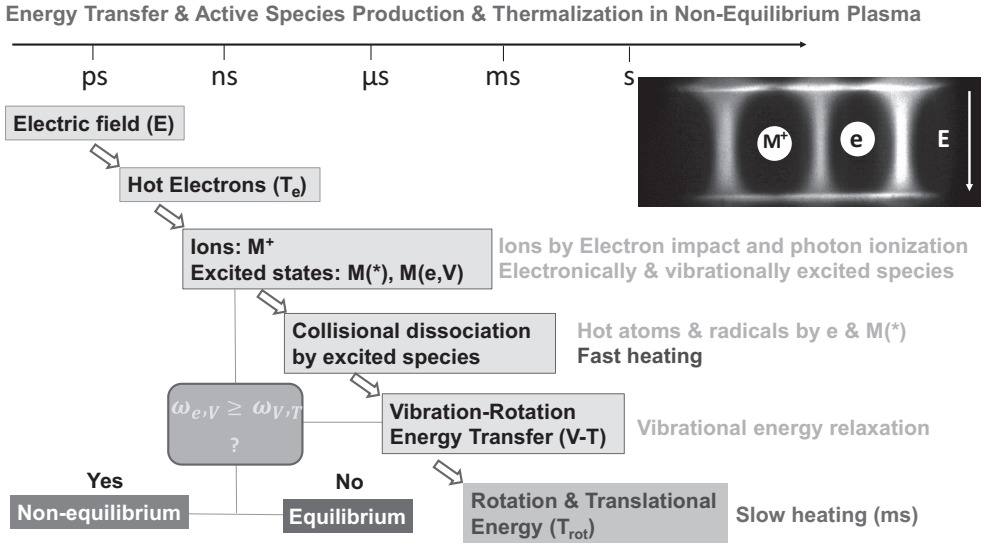

FIGURE 5.13 Timescales of nonequilibrium energy transfer, excitation, and relaxation in plasma and the production of ions, excited molecules, radicals, and heat via fast heating (via electrons and excited molecules) and slow heating processes (via V-V and V-T).

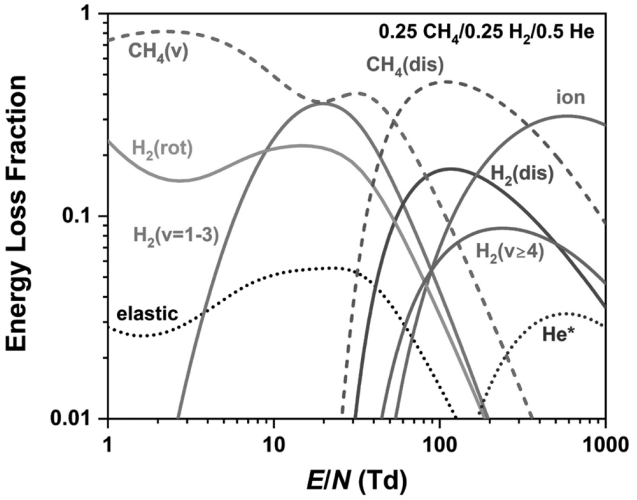

FIGURE 5.14 Computed energy loss fractions as a function of E/N in a methane/hydrogen/helium plasma.

to vibrational states of methane and hydrogen. However, when the E/N is increased above 50 Td, it is seen that CH_4 and H_2 dissociations and high-level H_2 vibrational excitation, H_2 ($v \geq 4$), will start to dominate. When the E/N is further increased above 100 Td, the ionizations of CH_4 and H_2 and the electronic excitations will dictate. Therefore, by controlling E/N, one can tune the active species production in plasma and control plasma chemistry for combustion and chemical manufacturing.

In the plasma-assisted combustion processes, the production of heat, chemically active species such as electrons, ions, vibrationally and electronically excited species, radicals, long-lifetime intermediate species, and fuel fragments as well as ionic wind and acoustic waves, and Coulomb and Lorentz forces, can affect the combustion process. Ju and Sun [90] summarized the three major pathways of the interactions between plasma and combustion, as shown in Figure 5.15. Plasma affects combustion via thermal, kinetic, and transport pathways. In the thermal enhancement pathway, the fast gas heating (due to rapid electronically excited state quenching) and slow gas heating (due to vibrationally excited state relaxation) from plasma increase temperature and accelerate chemical reactions and fuel oxidation according to the Arrhenius Law. In the kinetic enhancement pathway, high-energy electrons and photons are produced in plasma and lead to the production of active radicals (such as O, H, and OH) by direct electron impact and photo dissociation, ionization and recombination dissociation of ions (e.g., H_2^+ and O_2^+), and subsequent reactions involving electronically exited species (e.g. $O_2\left(a^1\Delta_g\right)$, N_2^* and $O(^1D)$) [91–94]. In addition, the long-lifetime

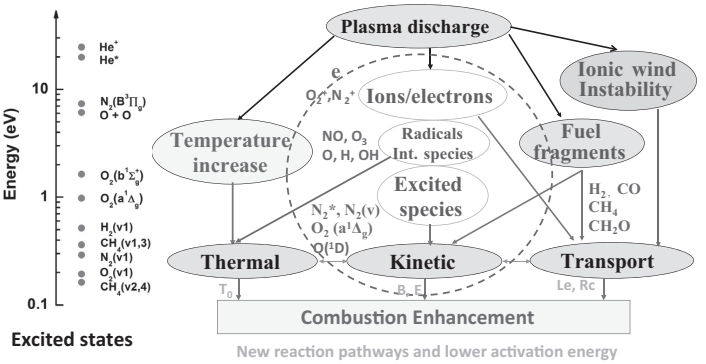

FIGURE 5.15 Schematic of major enhancement pathways of plasma-assisted combustion [90].

reactive (O_3) [95–97] and catalytic (NO) [70] intermediated species produced in the plasma also accelerate low-temperature fuel oxidation [78,79]. In the transport enhancement pathway, plasma dissociates the fuel molecules into fuel fragments, which changes the fuel diffusivity and therefore modifies the combustion process. In addition, the ionic wind as well as the acoustic waves, thermal expansion, and hydrodynamic instabilities produced by plasma can change the local flow velocity and increase the flow turbulence intensity and mixing.

In the sections below, we will discuss plasma chemistry and plasma-assisted combustion chemistry for hydrogen, methane, ammonia, and large hydrocarbons. In addition, the effects of a few key intermediate species produced in plasma such as ozone and NO_x on low-temperature fuel oxidation will be discussed.

5.2.2 Elementary Reactions of Plasma

Due to the electron-impact and photoionization processes in plasma (Figure 5.14), many chemically active species (Figure 5.15) are produced, and they will significantly affect plasma chemistry in combustion and manufacturing. These chemically active species need to be quantitatively quantified by using elementary reactions. Table 5.4 lists the major elementary reactions of electron-impact and photoionization processes in plasma. These processes include electron-impact excitation (electronically, vibrationally, and rotationally), electron-impact and photoionization to produce ions as well as new electrons, electron attachment and detachment, molecule dissociation by electrons and excited molecules, quenching of excited states, radiative and dissociative recombination, vibrational-vibrational energy transfer (V-V), and vibrational-translational (V-T) energy transfer. As shown in the representation reactions in the right column, these elementary processes govern the reactive energy transfer and chemically active species production.

TABLE 5.4
Elementary Reaction Processes via Electron Impact and Photon Ionization in Plasma

	Excitation of internal degrees of freedom	
$e + AB \rightarrow e + AB^*$	Electronic excitation	$e + N_2 \rightarrow e + N_2^*$
$e + AB \rightarrow e + AB(v)$	Vibrational excitation	$e + N_2 \rightarrow e + N_2(v)$
	Ionization	
$e + AB \rightarrow 2e + AB^+$	Ionization	$e + O_2 \rightarrow 2e + O_2^+$
$e + A^* \rightarrow 2e + A^+$	Multi-step ionization	$e + O(^1D) \rightarrow 2e + O^+$
$e + AB \rightarrow 2e + A + B^+$	Dissociative ionization	$e + N_2 \rightarrow 2e + N + N^+$
	Ionization	
$h\nu + AB \rightarrow AB^+ + e$	Photoionization	$h\nu + O_2 \rightarrow O_2^+ + e$
$nh\nu + AB \rightarrow AB^+ + e$	Multiphoton ionization	$nh\nu + O_2 \rightarrow O_2^+ + e$
	Attachment	
$e + AB \rightarrow A + B^-$	Dissociative attachment	$e + O_2 \rightarrow O + O^-$
$e + A + B \rightarrow A + B^-$	Three-body attachment	$e + O + O \rightarrow O + O^-$
	Detachment	
$A^- + B \rightarrow AB + e$	Detachment	$O + O^- \rightarrow O_2 + e$
	Dissociation	
$e + AB \rightarrow e + A + B$	Dissociation by electron	$e + H_2 \rightarrow e + H + H$

(*Continued*)

TABLE 5.4 (*Continued*)
Elementary Reaction Processes via Electron Impact and Photon Ionization in Plasma

$AB^* + CD \rightarrow AB + C + D$	Dissociation by excited molecules	$N_2^+ + H_2 \rightarrow N_2 + H + H$
	Quenching	
$e + A^* \rightarrow e + A$	De-excitation	$e + O(^1D) \rightarrow e + O$
	Recombination	
$e + e + A^+ \rightarrow e + A$	Three-body recombination	$e + e + O^+ \rightarrow e + O$
$e + AB^+ \rightarrow A + B$	Dissociative recombination	$e + O_2^+ \rightarrow O + O$
$e + A^+ \rightarrow A^* \rightarrow A + h\nu$	Radiative recombination	$e + O^+ \rightarrow O(^1D) \rightarrow O + h\nu$
	Vibrational energy transfer	
$AB(v = n) + CD(v = m) \rightarrow$	Vibrational-vibrational transfer (V-V)	$N_2(v = 1) + N_2(v = 1) \rightarrow$
$AB(v = n + 1) + CD(v = m - 1)$		$N_2(v = 2) + N_2(v = 0)$
$AB(v = n) + C \rightarrow AB(v = n - 1) + C$	Vibrational-translational transfer (V-T)	$N_2(v = 1) + O \rightarrow N_2(v = 0) + O$

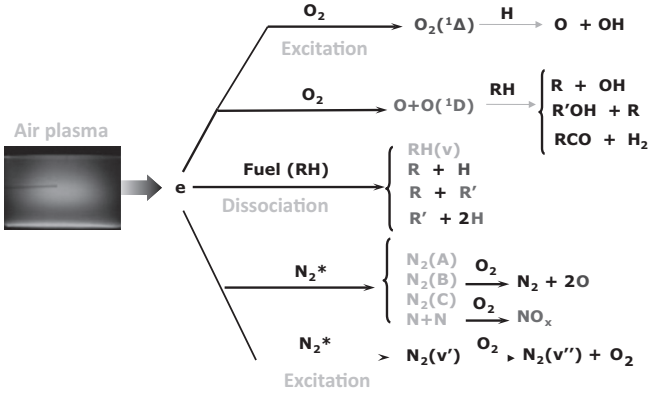

FIGURE 5.16 Schematic of chemically active species production via electron impact processes in an air/fuel mixture.

For example, in air plasma, the electron-impact excitation and dissociation of oxygen, nitrogen, and fuel (RH) molecules (Figure 5.16) will lead to many active species productions such as $O_2\left(a^1\Delta_g\right)$, $O(^1D)$, $N_2(A)$, $N_2(B)$, $N_2(C)$, $N_2(v)$, R, O, N, H, OH, and NO_x. Moreover, the reaction rates for this elementary process depend on the EEDF, thermal and non-thermal energy distributions of molecules, and the reaction cross-section areas. The production of active species will affect the chemical reactions in combustion and catalysis. Therefore, models for appropriate inclusion of these active species in plasma-assisted combustion and chemical manufacturing are needed.

In air plasma, in addition to the combustion species on the ground states, we also need to consider electronically excited states such as O_2^* (e.g., $O_2\left(a^1\Delta_g\right)$, $O_2\left(b^1\Sigma_g^+\right)$, $O_2\left(c^1\Sigma_u^-\right)$, $O_2\left(C^3\Delta_u\right)$, $O_2\left(A^3\Sigma_u^+\right)$); N_2^* (e.g., $N_2(A)$, $N_2(B)$, $N_2(a')$, $N_2(C)$), N^*(e.g., $N(^2D)$ and $N(^2P)$); O^* (e.g., $O(^1D)$ and $O(^1S)$); positive ions: O^+, O_2^+, O_4^+, N^+, N_2^+, N_3^+, N_4^+, NO^+, NO_2^+, N_2O^+; negative ions and charged particles: O^-, O_2^-, O_3^-, O_4^-, NO^-, NO_2^-, N_2O^-, e; vibrational states such as $O_2(v)$ and $N_2(v)$; and rotational states such as O_2(rot) and N_2(rot). All these species are chemically active species and their energy transfer and reactions with combustion species need to be appropriately considered in plasma-assisted combustion and chemical manufacturing. Note that depending on the chemical or combustion processes, not all these species and their associated reactions are equally important. Careful examination of the reaction pathways and

rate-limiting reactions for reactivity is needed. In the section below, we will provide a few examples of key elementary reactions in plasma-assisted combustion and fuel oxidation.

5.2.3 Elementary Reactions of Plasma-Assisted Hydrogen Combustion

Table 5.5 shows the key elementary reactions for radical production as well as fast and slow heating in the plasma-assisted hydrogen-air combustion system [90]. It includes the major electron-impact electronic and vibrational excitations, dissociation, and ionization, vibrational-translational (V-T) relaxation (slow heating), vibrational-vibrational (V-V) energy transfer, H abstraction of vibrationally excited species, dissociation by electronically excited species (fast heating), and electron-ion recombination.

Without plasma, as discussed in Section 5.1, the radicals (such as H and HO_2) are initially produced slowly by the chain-initiation reaction (R5.1). This process is very slow which makes hydrogen ignition delay time quite long even though it is a very reactive fuel. With plasma discharge, active radicals such as H, O, and OH will be produced in nanosecond timescale by electron-impact excitation and dissociation processes via reactions listed in Table 5.5. In addition, the V-T relaxation reactions (R5.14') generate slow heating between microsecond and millisecond. The dissociation reactions by excited species (R5.20'–R5.24') can not only produce radicals but also result in fast heating (via the extra energy of the excited states) from nanosecond to microsecond. Therefore, such rapid radical production and fast/slow heating in plasma will bypass the slow chain-initiation reaction (R5.1) and accelerate the chain-branching and propagation reactions (R5.3–R5.5) in hydrogen combustion, thus enhancing the combustion process.

Figure 5.17 [98–101] shows the comparison of the reaction rate of the key hydrogen chain-branching reaction (R5.3) at ground state with that when oxygen is electronically excited (R5.19'). It is seen that at low temperature (below 900 K), R5.19' is much faster than R5.3. Therefore, plasma-assisted chemical kinetics can dramatically accelerate ignition and combustion at low temperatures. Unfortunately, many reaction rates between the excited molecules with fuel molecules and intermediate species in combustion shown in Table 5.5 and Figure 5.16 remain unknown.

TABLE 5.5
Key Reactions in Plasma-Assisted $H_2/O_2/N_2$ Combustion System [90]

Electron Impact		**Vibrational-Translational (V-T) Relaxation: Slow Heating**	
$e + H_2 \rightarrow e + H_2(v = n)\,(n = 1-3)$	(R5.1')	$N_2(v = n) + H_2 \rightarrow N_2(v = n-1) + H_2$	(R5.14')
$e + O_2 \rightarrow e + O_2\ (v = n)(n = 1-4)$	(R5.2')	*Vibrational-vibrational (V-V) exchange*	
$e + N_2 \rightarrow e + N_2(v = n)\,(n = 1-8)$	(R5.3')	$N_2(v = n) + N_2(v = m) \rightarrow N_2(v = n-1) + N_2(v = m+1)$	(R5.15')
$e + O_2 \rightarrow e + O_2(a^1\Delta_g)$	(R5.4')	*H-abstraction of vibrationally excited species*	
$e + N_2 \rightarrow e + N_2(A)/N_2(B)/N_2(a')/N_2(C)$	(R5.5')	$O + H_2(v = n) \rightarrow OH + H\,(n = 1-3)$	(R5.16')
$e + H_2 \rightarrow e + H + H$	(R5.6')	$H_2(v = n) + OH \rightarrow H_2O + H\,(n = 1-3)$	(R5.17')
$e + O_2 \rightarrow e + O + O$	(R5.7')	$H + O_2(v = n) \rightarrow O + OH\,(n = 1-4)$	(R5.18')
$e + O_2 \rightarrow e + O + O(^1D)$	(R5.8')	*Dissociation by excited species: fast heating*	
$e + N_2 \rightarrow e + N + N(^2D)$	(R5.9')	$H + O_2(a^1\Delta_g) \rightarrow O + OH$ or HO_2	(R5.19')
$e + M \rightarrow e + e + M^+\ (M = H_2, O_2, N_2)$	(R5.10')	$O(^1D) + H_2 \rightarrow H + OH$	(R5.20')
Electron-ion recombination		$N_2(A)/N_2(B) + O_2 \rightarrow N_2 + O + O$	(R5.21')
$e + H_2^+ \rightarrow H + H$	(R5.11')	$N_2(a')/N_2(C) + O_2 \rightarrow N_2 + O + O(^1D)$	(R5.22')
$e + O_2^+ \rightarrow O + O/O(^1D)$	(R5.12')	$N_2(a') + H_2 \rightarrow N_2 + H + H$	(R5.23')
$e + N_2^+ \rightarrow N + N(^2D)$	(R5.13')	$N_2(C) + H_2 \rightarrow N_2 + H + H$	(R5.24')

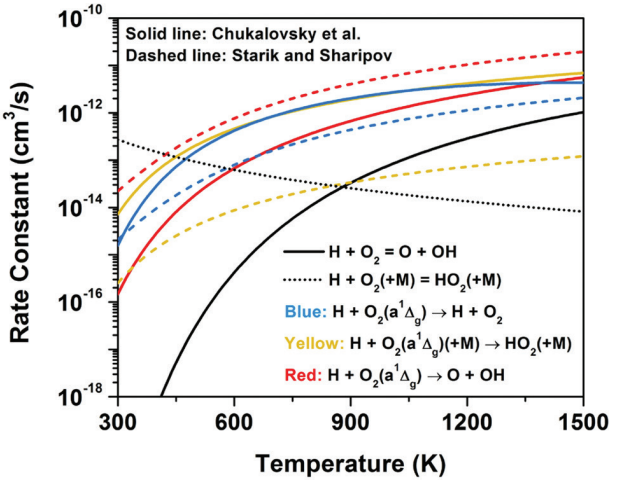

FIGURE 5.17 Reaction rate constants of different channels of $H+O_2\left(a^1\Delta_g\right) \rightarrow$ products from Chukalovsky et al. [102] and Sharipov and Starik et al. [100,101]. (Rate constant of the pressure dependence reaction $H+O_2\left(a^1\Delta_g\right)\ (+M) \rightarrow HO_2(+M)$ is presented at 1 atm as a second-order reaction.)

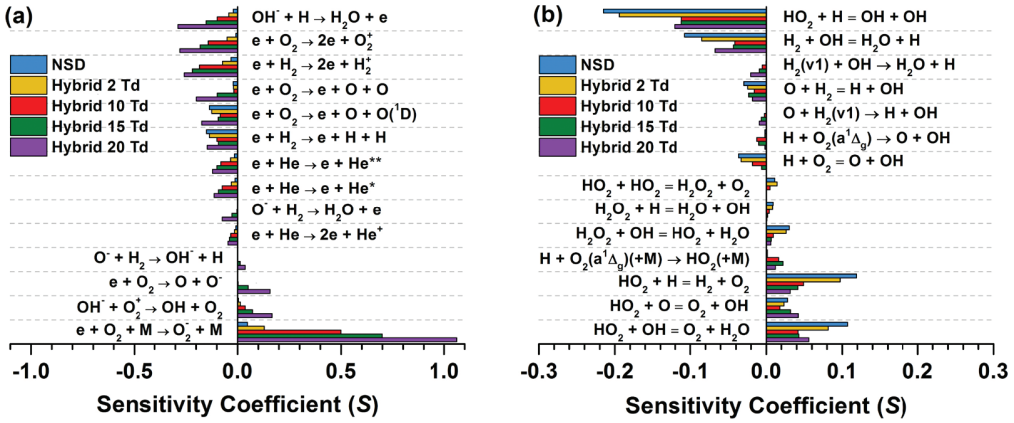

FIGURE 5.18 Sensitivity coefficients of the ignition delay time for NSD and hybrid discharge at different DC *E/N* values and 400 K, (a) electron impact reactions and (b) other reactions [99].

Figure 5.18 shows the sensitivity analysis of the ignition delay time of a H_2/O_2/He mixture for NSD and hybrid discharge with different DC reduced electric field strengths at 400 K [99]. For electron impact reactions, Figure 5.18 shows that $e+O_2 \rightarrow e+O+O(^1D)$ (R5.8') and $e+H_2 \rightarrow e+H+H$ (R5.6') are the dominant reactions in initial radical production and ignition enhancement in the NSD-assisted ignition. This figure clearly indicates the key roles of O, $O(^1D)$ and H production by plasma in combustion. In addition, it is seen that electron concentration and excited helium atoms also affect the production of excited species and radicals via $He^* + O_2 \rightarrow e + He + O_2^+$, $He^* + H_2 \rightarrow e + He + H_2^+$ and $He^{**} + He \rightarrow He_2^+ + e$ as well as $e+O_2 \rightarrow e+O+O$. Figure 5.18 also shows that the OH production reaction $HO_2+H=OH+OH$ has the largest sensitivity and plays a key role in the low-temperature H_2/O_2/He ignition. The major OH production is by $H_2(v1)$ and $O_2\left(a^1\Delta_g\right)$ via $O+H_2(v1) \rightarrow H+OH$, $H_2(v1)+OH \rightarrow H_2O+H$ and $H+O_2\left(a^1\Delta_g\right) \rightarrow O+OH$. This plasma kinetic enhancement of hydrogen combustion suggests that plasma is a promising tool to actively control combustion.

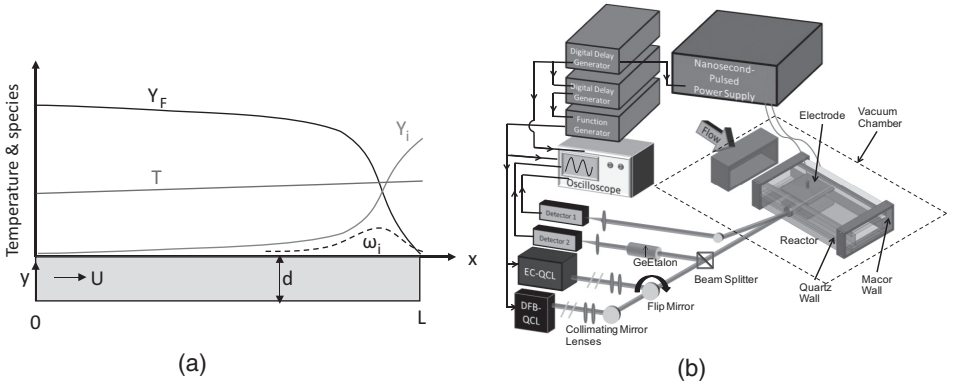

FIGURE 5.19 (a) Schematic of species and temperature distribution in a flow reactor. (b) Schematic of experimental setup for DBD flow reactor with TDLAS measurement system.

To obtain time-resolved species measurements and validated kinetic models, Lefkowitz et al. [103–105] developed a plasma reactor with *in situ* optical diagnostics (see Figures 9.11 and 9.12). This reactor (Figures 9.11 and 9.12) has been used to develop plasma-assisted combustion model for H_2 [99], CH_4 [105], C_2H_4 [104], C_5H_{12} [106], n-heptane [107], n-dodecane [108], and NH_3 [109]. Figure 5.19 provides a schematic of the experimental setup. The reactor is constructed primarily of quartz and Macor, with a stainless-steel inlet gas flow manifold and brackets. Each of the two 45 mm×45 mm stainless-steel electrodes is sandwiched between a quartz plate and a Macor plate which make up the top and bottom of the reactor, forming a plane-to-plane double DBD. There is a wedge-shaped calcium fluoride window in the sidewall to allow the mid-IR laser beam to pass through the chamber wall and into the Herriott cell for laser absorption measurements. All experiments were conducted at a total pressure of 30–100 Torr and an initial temperature of 296 K.

To make kinetic measurement in a reactor, an important assumption is that the flow reaction system is either a time-evolving zero-dimensional or a steady-state one-dimensional plug flow reactor. In the formal case, the distribution of species and temperature in the reactor needs to be homogeneous, so that the species and energy governing equation can be written as

$$\frac{dY_i}{dt} = \frac{\omega_i}{\rho} \tag{5.5a}$$

$$\frac{dT}{dt} = -\sum_i \frac{\omega_i h_i}{\rho C_p}, \; i = 1 \ldots N \tag{5.5b}$$

Therefore, by measure the time history of *i*th species mole fraction, Y_i, and temperature, T, the reaction rate of ω_i can be validated.

In the steady-state one-dimensional plug flow reactor, two assumptions need to be valid: (1) the ratio of the diffusion time (d^2/D_i) to the flow residence time ($\tau_{res}=L/U$) is very small (d is the reactor's channel height) so that the diffusion in the direction vertical to the flow is fast so that the concentration and temperature gradient $dY_i/dy \approx 0$. (2) The diffusion flux in the flow direction is negligible, and (3) the reaction Damköhler number is close to unity

$$D_a = \frac{\tau_{\text{res}}}{\tau_r} = \frac{\tau_{\text{res}}}{\rho/\omega_i} \approx 1 \tag{5.6}$$

With the above three assumptions, the governing equations for energy and species in the coordinate of the flow direction normalized by the length of the reactor (L) in Figure 5.19a can be given as,

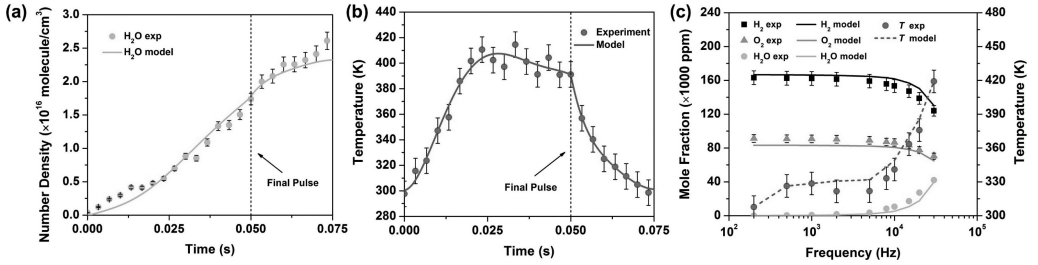

FIGURE 5.20 Time-dependent measured (a) H_2O number density and (b) temperature with fitted line with model prediction during and after the 1,500 pulse, 30 kHz nanosecond plasma in a burst mode; and (c) species concentration between steady-state measurement and model prediction as well as measured temperature in a continuous nanosecond plasma ranging from 200 Hz to 30 kHz for a 0.1667 H_2/0.0833 O_2/0.75 He mixture at 60 Torr [99].

$$\frac{dY_i}{dx} = \tau_{\text{res}} \frac{\omega_i}{\rho} \tag{5.7a}$$

$$\frac{dT}{dx} = -\tau_{\text{res}} \sum_i \frac{\omega_i h_i}{\rho C_p}, \; i = 1 \ldots N \tag{5.7b}$$

We will use the plasma flow reactor to study plasma chemistry. The purpose of the studies was to quantitatively measure time-resolved species production and temperature histories in a homogeneous plasma discharge and compare these results with kinetic modeling.

By using experiments in Figure 5.19 and the kinetic model in Table 5.5 by including helium, Mao et al. [99] studied the plasma-assisted low-temperature H_2/O_2/He combustion kinetics in a repetitively-pulsed nanosecond discharge (NSD). Figure 5.20a and b show the time-dependent measurement of H_2O number density and temperature measured *in situ* by mid-IR tunable diode laser absorption spectroscopy (TDLAS) during and after the 1,500 pulse, 30 kHz nanosecond plasma in a burst mode. Figure 5.20a shows that the H_2O number density increases with discharge pulses from room temperature due to the O and H radicals as well as electronically excited O(^{1}D) produced by electron-impact dissociation reactions (R5.6'–R5.8'). With the progress of hydrogen oxidation, the temperature increases with plasma pulses as shown in Figure 5.20b. Note that the temperature peaks at the end of the discharge burst and decreases after that due to heat losses from the discharged mixture to the reactor walls. Figure 5.20c shows the species concentration measured *ex situ* by gas chromatograph (GC) measurements and temperature as a function of pulse repetition frequency. It is seen that the fuel consumption and temperature increase with the plasma frequency as more energy is deposited into the plasma with more pulses. In addition, the model prediction agrees well with the experimental data. Therefore, the development of experimentally validated kinetic models is critical for plasma modeling.

5.2.4 Kinetics of Plasma-Assisted CH_4 Combustion

Plasma-assisted methane oxidation plays a critical role in fuel flexible power generation, heating, and methane reforming. Previous studies of methane oxidation in plasma have been conducted using shock tubes [110–112], counterflow flames [113,114], and flow reactors [115–118]. In addition, there have been extensive studies of plasma fuel reforming using methane [119–127]. In shock tubes, Kosarev et al. [110] measured ignition delays after a fast ionization wave (FIW) in CH_4/O_2/Ar mixtures at initial temperatures from 1,230 to 1,719 K and pressures from 0.3 to 1.1 bar. It was shown that the ignition delay was shortened by a factor of 30 using a nanosecond pulsed plasma.

Lou et al. [115] studied the oxidation of methane-air mixtures in a NSD in a homogenous flow reactor at initial temperature of 290 K and pressure <100 Torr. The results showed that PAC could accelerate fuel oxidation. Further studies of plasma-assisted methane combustion [116–118] quantitatively measured the temperature, NO, O, and OH concentrations. Modeling of the PAC processes predicted the temperature and O-atom concentration, but different combustion kinetic models had mixed results in predicting the OH profile. In counterflow flames, Sun et al. [113,114] found that the extinction limits of a partially premixed $CH_4/O_2/Ar$ mixture could be extended by more than a factor of two when a nanosecond pulsed discharge was applied to the mixture at the exit of the fuel nozzle. Modeling efforts found that O and CH_2O concentrations were well predicted, but the concentration of H_2, CO, CO_2, and H_2O could not be matched by the model predictions. It was found that methane ignition was significantly accelerated by plasma at high oxygen concentrations.

However, few quantitative comparisons between measured and predicted time histories of species concentrations were made. Therefore, experimentally validated kinetic models for quantitatively predicting plasma-assisted methane combustion remain scarce. The model predictability, especially at low temperature, in terms of speciation data, is still limited, preventing a full assessment of the reaction pathways and computational design optimization of the reaction systems.

Recently, Lefkowitz et al. [105] measured plasma-assisted methane oxidation using the reactor in Figure 5.19 and conducted time-dependent and *in situ* measurements of reactants, products, and intermediate species as well as temperature. Figure 5.21 presents the mole fraction of CH_2O, a key low-temperature intermediate species of methane oxidation, as a function of time [105]. The model under-predicted the peak concentration of CH_2O by a factor of 5, indicating a major limitation in the model's predictive ability of this primary intermediate in low-temperature plasma-assisted methane oxidation. The primary formation pathways reported for CH_2O in methane PAC [110,128] are as follows:

$$CH_3 + O \rightarrow CH_2O + H \qquad \text{(R5.58)}$$

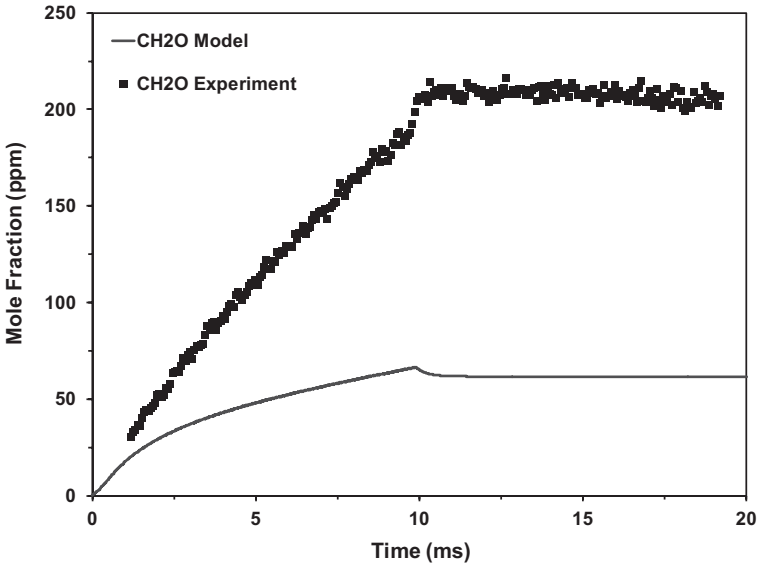

FIGURE 5.21 Formaldehyde measurement and model prediction during and after a 300 pulse burst plasma discharge at 30 kHz repetition rate and 8.76 kV peak voltage in a stoichiometric $CH_4/O_2/He$ mixture with 75% dilution [105].

$$O(^1D) + CH_4 \rightarrow CH_2O + H_2 \quad \text{(R5.25a')}$$

in which CH_3 is mainly produced via,

$$O(^1D) + CH_4 \rightarrow CH_3 + OH \quad \text{(R5.25b')}$$

$$e + CH_4 \rightarrow e + CH_3 + H \quad \text{(R5.26a')}$$

and O is formed from R5.7' and R5.8' by electron-impact oxygen dissociation. The discrepancy between experimental data and model prediction indicates that the reaction rates of Eqs. R5.25' and R5.26a' may not be properly modeled.

To collect a more complete set of species data, multiple species quantification was also made by using a gas chromatograph and temperature measurements were conducted by two-line laser absorption spectroscopy. Figure 5.22 presents measured and predicted species concentrations as a function of the NSD frequency. Figure 5.22a presents the concentrations of the reactants and H_2O. It is found that the fuel and oxygen consumption are predicted to be within 5% of the measured values. Therefore, the total electron collision rates were well modeled. The production of water is predicted within 20% of the measured value, which is in excellent agreement. Figure 5.22b presents the other major products: carbon monoxide, carbon dioxide, and hydrogen. The model captures the correct trends and relative concentrations of the three species, but under-predicts the absolute concentrations, particularly at the highest frequency conditions. The minor species are plotted in Figure 5.22c. Agreement is comparatively poor between the model and measurements of formaldehyde, methanol, ethane, ethylene, and acetylene. Like the time-dependent results, formaldehyde is under-predicted by approximately a factor of five, while methanol is over-predicted by an order of magnitude. In summary, the major trends of reactant consumption and major product species production are well captured by the kinetic model, indicating that the electron collision rates and dominant reaction pathways are well modeled, but the minor intermediate species modeling results are in significant disagreement, indicating that perhaps some secondary rates need further attention.

To understand which reaction pathways are of importance, Figure 5.23 presents the consumption pathways of methane for 30 kHz continuously pulsed plasma at steady-state temperature as predicted by the model. The major fuel consumption pathways are through electron collision reactions, reactions with $O(^1D)$, and reaction with OH.

Reactions R5.25a', R5.26a' and $CH_4 + OH = CH_3 + H_2O$ are the major reaction pathways (64%) for methane consumption. The electron-impact dissociative excitation reactions via R5.26a' and

$$e + CH_4 \rightarrow e + CH_2 + H_2 \quad \text{(R5.26b')}$$

$$e + CH_4 \rightarrow e + CH + H_2 + H \quad \text{(R5.26c')}$$

also account for 16% of CH_4 consumption, while electron-impact ionization and dissociative ionization reactions of $e + CH_4 \rightarrow 2e + CH_4^+$ and $e + CH_4 \rightarrow 2e + H + CH_3^+$ reactions account for 20%. The CH_4 dissociative excitation reactions of R5.26' lead to methyl radical (CH_3) and methylene radical (CH_2) formation, while the dissociative ionization reaction leads to methyl cation (CH_3^+). About 10% of CH_4 consumption leads to CH_2 radical production. At low temperature, the CH_2 radical is then oxidized by reactions with oxygen,

$$CH_2 + O_2 = CO + OH + H \quad \text{(R5.59a)}$$

$$= CO_2 + H + H \quad \text{(R5.59b)}$$

$$= CO_2 + H_2 \quad \text{(R5.59c)}$$

$$= CH_2O + O \quad \text{(R5.59d)}$$

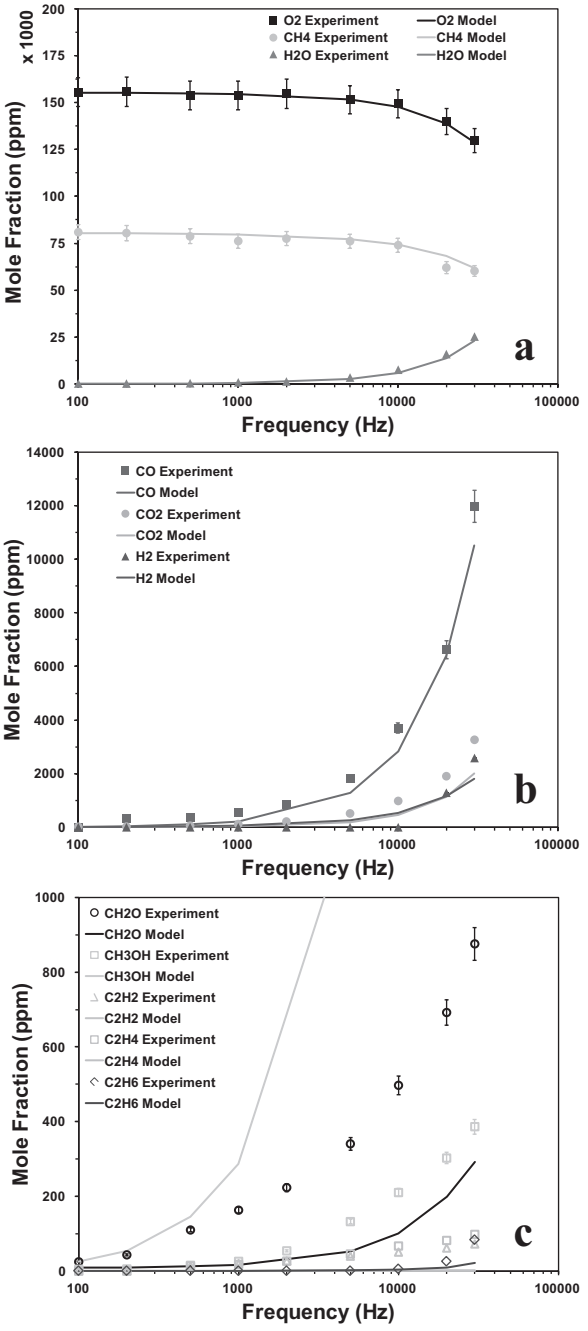

FIGURE 5.22 Species measurements and model predictions in a continuous plasma at 30 kHz repetition rate and 8.76 kV peak voltage in a stoichiometric CH_4/O_2/He mixture with 75% dilution [105].

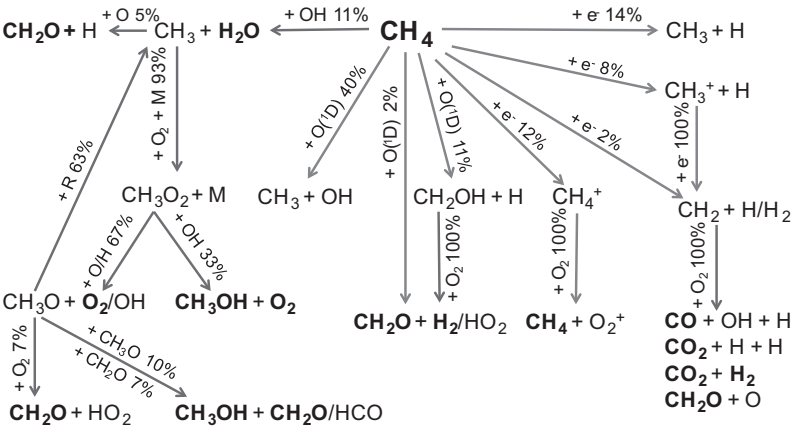

FIGURE 5.23 Path flux analysis of formaldehyde and methanol formation integrated over a single pulse period during continuous discharge at 30 kHz repetition frequency and steady-state temperature conditions. Bold species represent those which are measured in the experiment, red arrows refer to reactions from the combustion model, and blue arrows are from the plasma model. R represents any radical species.

resulting in the formation of CO, CO_2, and CH_2O. Reaction R5.59a accounts for 47% of carbon monoxide formation, and reactions R5.59b and R5.59c together account for 99% of carbon dioxide formation from CH_2. Reaction R5.59c accounts for 19% of hydrogen formation, while the dissociative excitation of methane (R5.26') accounts for another 35% of hydrogen production, thus accounting for a total of 54% of the hydrogen formation together. All three species are reasonably well predicted by the model.

In low-temperature plasma discharge, methyl radical is consumed by O and O_2 via,

$$CH_3 + O = CH_2O + H \tag{R5.60}$$

$$CH_3 + O_2 + M = CH_3O_2 + M \tag{R5.61}$$

The competition between these two reactions determines the production of methanol (Figure 5.6), as R5.61 leads to methyl peroxy radical (CH_3O_2) formation, which reacts with small radicals to form CH_3OH and CH_3O via reactions (Figure 5.6),

$$CH_3O_2 + OH \rightarrow CH_3OH + O_2 \tag{R5.62}$$

$$CH_3O_2 + H \rightarrow CH_3O + OH \tag{R5.63}$$

$$CH_3O_2 + CH_3 \rightarrow 2CH_3O \tag{R5.64}$$

$$CH_3O_2 + O \rightarrow CH_3O + O_2 \tag{R5.65}$$

Reaction R5.62 is responsible for 82% of methanol formation, while further reactions from CH_3O contribute to the remaining 18% of methanol formation, as presented in Figure 5.23.

To understand how the LTC in plasma-assisted combustion plays a critical role in model prediction, Figure 5.24 compares the experimental results and predictions by using two different models,

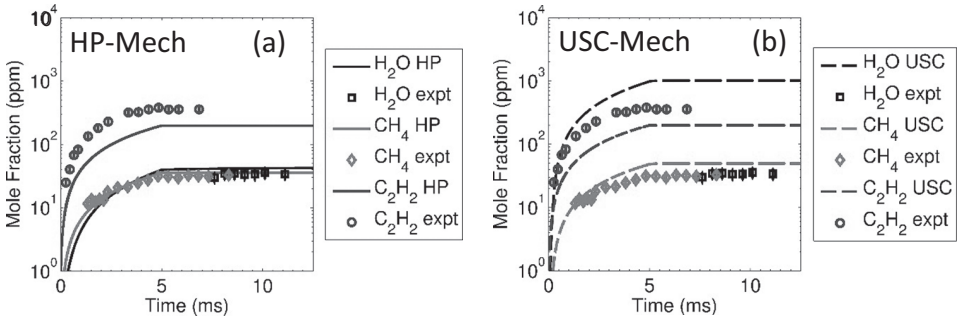

FIGURE 5.24 Measurements and predictions of C_2H_2, CH_4, and H_2O concentrations after 150 pulses at 30 kHz repetition rate for a mixture of $C_2H_4/O_2/Ar$: 6.25/18.75/75 by using (a) HP-Mech and (b) USC-Mech II [104].

HP-Mech [104] and USC-MECH [129], for plasma-assisted ethylene oxidation. The former includes the low-temperature reaction pathway discussed above and the latter only has high-temperature reaction pathways. It is clearly seen that the high-temperature model poorly predicts the formation of major products H_2O, C_2H_2, and CH_4.

Therefore, in plasma-assisted low-temperature methane oxidation, the reaction channels via CH_3O_2 and CH_3OH need to be appropriately included (Figure 5.6). In addition, some reaction channels for CH_2O may still be missing or inaccurate in the rate constants. Future studies are still needed.

5.2.5 Kinetics of Plasma-Assisted NH_3 Combustion and NO_x Emissions

Ammonia (NH_3) is considered to be an important hydrogen carrier for power generation [5,130,131] and distributed energy storage [132]. However, ammonia is difficult to ignite, has very low flame speeds, and high N_2O/NO_x emissions. The low reactivity of ammonia at low temperatures creates serious concerns of incomplete NH_3 combustion resulting from cold engine walls and poor fuel/air mixing. The unburnt ammonia emitted into the atmosphere will change the nitrogen cycle and contribute to smog formation due to the strong coupling of HO_x–NO_x–VOC–O_3 chemistry [133]. As such, enhancing low-temperature ammonia oxidation as well as controlling N_2O/NO_x emissions by using plasma is of paramount significance.

Recently, several research efforts have been devoted to plasma-assisted ammonia combustion. Studies in high-temperature ammonia flames [134–136] reported encouraging impacts of plasma on enhancing combustion and reduction in NO. However, the underlying nonequilibrium plasma kinetics for ammonia oxidation are not well understood. Several key technical questions remain to be answered: How will plasma chemistry affect ammonia oxidation and NO_x emissions? What are the major ammonia and NO_x reaction pathways in plasma? Unfortunately, few experimentally validated models exist.

More recently, Zhong et al. [137] conducted *in situ* diagnostics of nonequilibrium ammonia oxidation and developed an experimentally validated N_2O/NO_x chemistry in low-temperature plasma. The experimental setup is shown in Figure 5.25.

The plasma reactor is a rectangular flow reactor and is the same as that in Figure 5.19. The reactor is maintained at 30 Torr and the overall flow velocity was 0.3 m/s (the residence time is 0.15 s). The nanosecond (ns) voltage pulser operates repetitively in both burst and continuous modes. The burst mode was used to facilitate the time-dependent species production. The burst frequency was 0.2 Hz. Each burst had 400–600 pulses running at 30 kHz with a peak voltage of 11 kV and pulse duration of ~20 ns. TDLAS was used to scan two NH_3 lines at 1726.39 cm^{-1} and 1727.09 cm^{-1} for both temperature and concentration measurements. Two distributed feedback quantum cascade

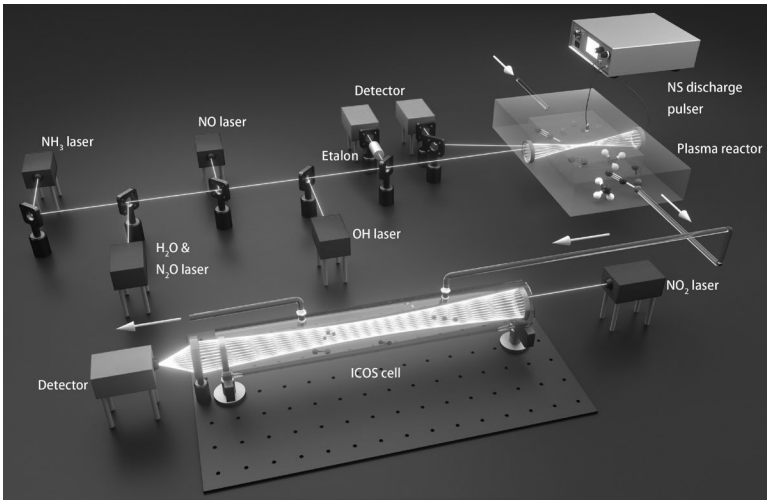

FIGURE 5.25 Experimental setup of ammonia oxidation in a plasma reactor with time-resolved laser diagnostics [137].

lasers (DFB QCLs) were used for NO and OH measurements at 1906.73 and 3568.41 cm^{-1}, respectively. An external-cavity QCL was also used for the detection of H_2O at 1338.55 cm^{-1} and N_2O at 1306.93 cm^{-1}. In addition, a sensitive off-axis integrated cavity output spectroscopy (ICOS) [93] was employed for NO_2 measurement at 6640.4 cm^{-1}.

A $NH_3/O_2/N_2$ plasma-combustion kinetic model was assembled and updated. The vibrationally excited species NH_3 ($v=1$–4), O_2 ($v=1$–4), N_2 ($v=1$–8); electronically excited species $O_2\left(a^1\Delta_g\right)$, $O_2\left(b^1\Sigma_g^+\right)$, $O(^1D)$, $O(^1S)$, $N_2(A)$, $N_2(B)$, $N_2(a')$, $N_2(C)$, $N(^2D)$; ions NH^+, NH_2^+, NH_3^+, NH_4^+, N_2H^+, O_2^+, O_4^+, N_2^+, N_4^+, H_2^+, H_3^+, H_2O^+, H_3O^+, O^-, O_2^-, O_4^-, OH^-; and electrons were included in the model. Both V-T and V-V energy transfers were considered. The reaction cross-section area data of electron impact reactions of NH_3, O_2, and N_2 were obtained from the database LXCat [138]. The NH_3 oxidation sub-mechanism was taken from Thorsen et al. [35] and the O_3 sub-mechanism of Zhao et al. [139] was added. This is the "Starting Model". Based on the experimental data, the electron impact cross sections of

$$e + NH_3 \rightarrow e + NH + H_2 \tag{R5.27a'}$$

and the rate constants of $N_2(a')$ and $N_2(C)$ with NH_3 dissociation reactions,

$$N_2\left(a'\right) + NH_3 \rightarrow N_2 + NH_2 + H \tag{R5.28a'}$$

$$N_2\left(a'\right) + NH_3 \rightarrow N_2 + NH + H_2 \tag{R5.28b'}$$

$$N_2(C) + NH_3 \rightarrow N_2 + NH_2 + H \tag{R5.29a'}$$

$$N_2(C) + NH_3 \rightarrow N_2 + NH + H_2 \tag{R5.29b'}$$

were adjusted to fit the experimental data. In addition, several reaction rates involving NH and NH_2 reactions with NO and HO_2 were also changed within the uncertainty of these reactions to fit the

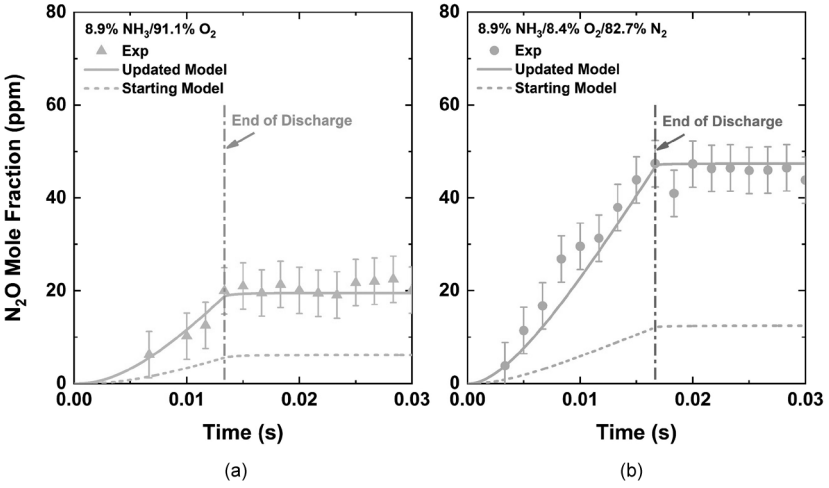

FIGURE 5.26 Nitrous oxide (N_2O) measurements (scatter) and model predictions (lines) during and after a train of plasma pulse burst at 30 kHz repetition rate: (a) without (400 pulses) and (b) with N_2 dilution (500 pulses). The vertical line indicates the end of the plasma discharge.

experimental measurements. This updated model is labeled as the "Updated Model" in the following comparison. The final kinetic model consists of 77 species and 894 reactions.

Figure 5.26 shows the comparisons of measured and computed time-dependent N_2O profiles. Significant amount of N_2O was formed at room temperature after hundreds of discharge pulses. Note that the Starting Model fails to predict N_2O formation by one order of magnitude.

Important reaction pathways for ammonia oxidation, NO, NO_2, and N_2O formation as well as NO reburning ($DeNO_x$) are shown in Figure 5.27. Like NH_3 combustion, the major oxidation sequence from NH_3 to NO in low-temperature plasma is,

$$NH_3 \rightarrow NH_2 \rightarrow HNO \rightarrow NO \tag{R5.66}$$

First, NH_3 is dissociated by electron impact via R5.27' and the collisions with electronically excited N_2(A, B, a', C) via R5.28' and R5.29'. In addition, R5.27 as well as the H-abstraction reactions from NH_3 by $O(^1D)$ and $N(^2D)$,

$$e + NH_3 \rightarrow e + NH_2 + H \tag{R5.27b'}$$

$$O\left(^1D\right) + NH_3 \rightarrow NH_2 + OH \tag{R5.30'}$$

$$N\left(^2D\right) + NH_3 \rightarrow NH + NH_2 \tag{R5.31'}$$

also contribute to NH_3 consumption. NH_2 is then mainly consumed by R5.29 to form HNO. Finally, HNO is converted to NO by reacting with H and O produced in plasma via HNO + H = NO + H_2 and HNO + O = NO + OH. Therefore, plasma-generated electrons and excited species accelerate NH_3 dissociation and NO formation via radical production of O/H/N (on the left in Figure 5.27). Note that most NO is formed from NH and NH_2, and only 2% of NO is formed directly through N atom via,

$$N\left(^2D\right) + O_2 \rightarrow NO + O\left(^1D\right) \tag{R5.32a'}$$

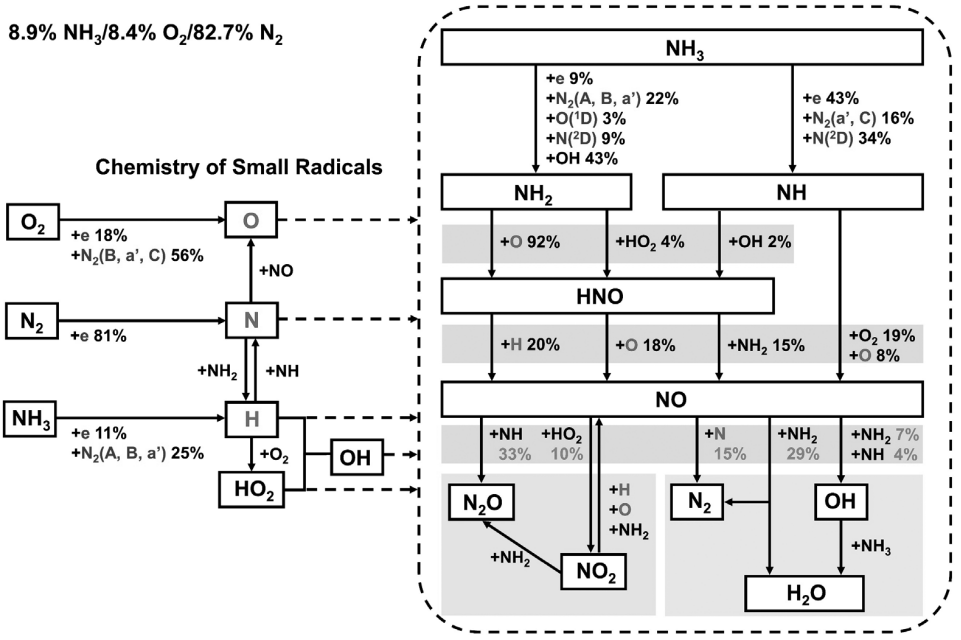

FIGURE 5.27 Path flux analysis of plasma-assisted ammonia oxidation and NO_x formation. Species in purple indicate nonequilibrium species directly generated by plasma. The three blue shading in the right block indicates the major path flux for HNO formation, NO formation, and NO consumption. The orange shading in the right figure indicates NO_x coupling. The green shading in the right figure indicates NH_3 oxidation. The percentages with black (green) color indicate the contributions accounting for the species total production (consumption).

$$N(^2D) + O_2 \rightarrow NO + O \qquad \text{(R5.32b')}$$

Figure 5.27 also shows that NO formed in plasma-assisted low-temperature ammonia combustion is either converted to N_2O, NO_2, or N_2 ($DeNO_x$ mechanism). One major channel of NO consumption is NO_2 by

$$NO + HO_2 = NO_2 + OH \qquad \text{(R5.41)}$$

The other NO consumption channels are conversions to NNH, N_2, and N_2O by NH_x through the thermal $DeNO_x$ mechanism,

$$NO + NH_2 = NNH + OH \qquad \text{(R5.24a)}$$

$$NO + NH_2 = N_2 + H_2O \qquad \text{(R5.24b)}$$

$$NO + NH = N_2O + H \qquad \text{(R5.32a)}$$

$$NO + NH = N_2 + OH \qquad \text{(R5.32b)}$$

This $DeNO_x$ mechanism plays a critical role in the development of NO_x reduction strategies for low-temperature ammonia oxidation.

For N_2O formation in low-temperature plasma-assisted ammonia oxidation, in addition to R5.32, it is also formed from NO_2 via,

$$NH_2 + NO_2 = N_2O + H_2O \quad \text{(R5.42b)}$$

Therefore, the NO_x formation in low-temperature plasma discharges follows a two-step mechanism (Figure 5.27). The first step is solely controlled by nonequilibrium plasma chemistry, where electron-impact ammonia dissociation and the collisional quenching of excited species provide amine radicals and O/H/OH/HO_2 radicals. The second step is the reactions between amine radicals and O/H/OH/HO_2 which lead to NO and NO_2 formation. N_2O is then formed from NO and NO_2 by the amine radicals produced in the plasma. Unfortunately, the rate constants for amine radical production via electronically excited nitrogen, nitrogen atom, and oxygen atom are not well determined. Future studies in these reactions are needed to improve the model predication.

5.2.6 Kinetics of Plasma-Assisted Large Hydrocarbon and Oxygenate Fuel Combustion

For hydrogen, methane, and ammonia plasma-assisted combustion, the major role of plasma is to generate radicals from electron-impact and excited molecules to accelerate the chain-initiation reaction R5.1 and then to promote the onset of the high-temperature chain-branching reaction R5.3. However, for large hydrocarbons or oxygenates, as discussed in Section 5.1.5, in addition to the high-temperature chain-branching reaction R5.3, the low-temperature and intermediate temperature chain-branching pathways via R5.56 and R5.57 are also important. These reactions have lower activation energy than R5.3. The question then becomes at what temperature plasma-assisted radical production can accelerate the low-temperature chain-branching reactions and at what electric field strength?

Figure 5.28a shows a comparison of the radical production reaction flux of the electron-impact atomic oxygen and O(^{1}D) production (R5.8') as a function of the reduced electric field for reaction in comparison with that of important chain-branching and propagation reactions (R5.1–R5.5). Although the rate constant of the electron-impact reaction is much larger than that of the important radical chain-branching and initiation reactions, the reaction flux at a typical flame condition (the estimation condition of 1 atm, the electron number density of $5\times10^{11}\,cm^{-3}$, O and H at $4.9\times10^{15}\,cm^{-3}$, O_2 concentration at 19%, H_2 concentration of 0.5%, and H_2O_2 concentration of 500 ppm) [90] for the electron-impact reaction is only faster than that of the key combustion reactions at low temperatures ($T<1{,}100$ K). Therefore, at low temperatures, plasma can effectively enhance combustion by accelerating the chain-initiation, branching, and propagation reactions

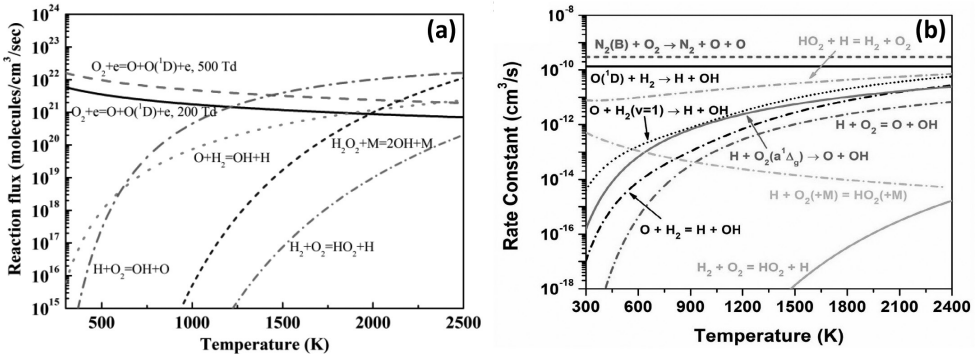

FIGURE 5.28 (a) Comparison of reaction flux between electron impact oxygen dissociation reaction and key chain-initiation and termination reactions of hydrogen. (b) Comparison of rate constants of oxygen and hydrogen dissociation reactions with key hydrogen elementary reactions [90].

R5.1–R5.5. However, when the temperature is higher than 1,100 K, the high-temperature combustion chain-branching reaction (R5.3) starts to dominate the radical production process. Note that for almost all the flames, their temperatures are higher than 1,100 K because of the rate-limiting reaction of R5.3. Therefore, the plasma effect on combustion at temperature above 1,100 K is more through the thermal effect (e.g., for flames) or bypassing the chain-initiation reaction (R5.1) (e.g., for ignition) than the kinetic enhancement.

Figure 5.28b shows the rate constants of key combustion reactions with H_2, N_2, O, and O_2 on the ground states in comparison to that of similar reactions at their vibrationally and electronically excited states as a function of temperature. It is seen that the rate constants of reactions involving vibrationally ($H_2(v=1)$) and electronically ($O_2\left(a^1\Delta_g\right)$, $O(^1D)$ and $N_2(B)$) excited species are several orders of magnitude higher than that of the combustion chain-initiation and chain-branching reactions, especially at low temperatures. Therefore, in plasma, in addition to the electron-impact reaction R5.8', the radical production reactions involving vibrationally and electronically excited molecules and ions (R5.14'–R5.21') will also help to kinetically accelerate fuel oxidation at low and intermediate temperatures.

To schematically show how plasma-assisted radical production in ignition of large hydrocarbons and oxygenated fuels, Figure 5.29 shows schematically the two-stage ignition, LTI and HTI, the plasma-assisted radical production, and the radical production via the major reaction pathways of combustion at low, intermediate, and high temperatures, respectively, via R5.56, R5.57, and R5.3. It is important to bear in mind that, at high temperature (above 1,100 K), when the temperature is above the critical temperature of the chain-branching reactions (R5.3), the major role of plasma is thermal enhancement or the chain-initiation enhancement (R5.1) because the branching rate of R5.3 is very high. As the temperature reduces, however, the kinetic effect of plasma chemistry on ignition plays an increasing role to accelerate ignition at low and intermediate temperatures to promote the chain-branching reactions R5.56 and R5.57. As discussed in Figure 5.11, radical production by plasma can accelerate LTI by one order of magnitude. Such significant enhancement is because at low temperature, the radical production by plasma is much faster than the rate-limiting chain-branching reactions R5.48–R5.51 at low temperature and R5.5 at intermediate temperature. As will be discussed in later sections, because of the significant plasma kinetic enhancement at low temperature, one can observe stable cool flames in laboratory even at atmospheric pressure.

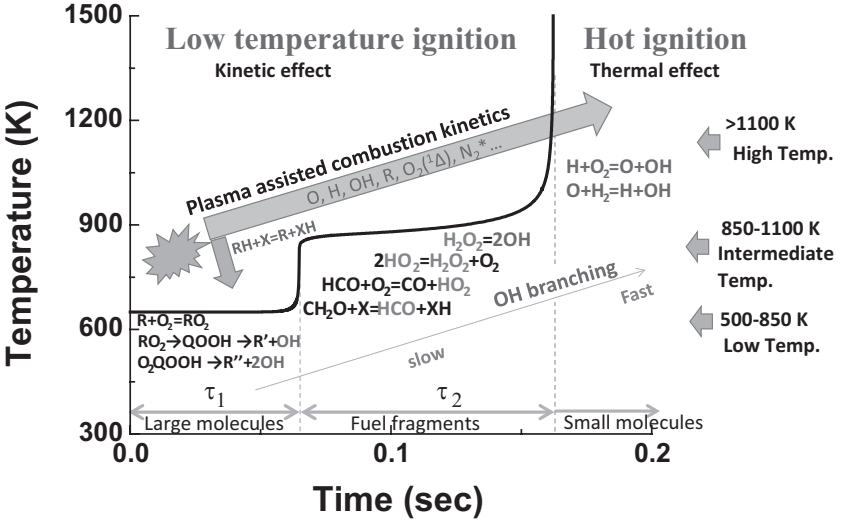

FIGURE 5.29 Schematic of kinetic and thermal enhancement pathways of plasma-assisted combustion for liquid fuels at high, intermediate, and low temperatures, respectively [90].

To develop experimentally validated kinetic models, plasma reactor experiments (Figure 5.19) were carried out for large n-alkanes (pentane, heptane, and dodecane) [106–108]. Here we will use n-dodecane as an example for the development of experimentally validated kinetic models and discuss what needs to be done in the future.

Both plasma-assisted pyrolysis and oxidation of n-dodecane were conducted using the same plasma reactor in Figure 5.19. In the pyrolysis case, 1% n-dodecane and 99% N_2 were used as the reactant mixture. In the oxidative case, 1% n-dodecane, 19% oxygen, and 80% N_2 were flown into the system. For *in situ* measurements of species-time profiles, a 24-pass Herriott multi-pass cell was utilized for mid-IR TDLAS measurements. An absorption line at 1,377 cm^{-1} was chosen for n-dodecane with calibration. Time-resolved measurements of other species such as CH_4 at 1341.62 cm^{-1}, C_2H_2 at 1342.35 cm^{-1}, and H_2O at both 1338.55 cm^{-1} and 1339.15 cm^{-1} were also conducted using EC-QCL. CH_2O was quantified at 1726.79 cm^{-1} using a DFB laser. For steady-state measurements, a gas chromatograph (GC) was used. A dual-modulation Faraday rotation spectroscopy (DM-FRS) system [140,141] was developed to detect steady-state nitric oxide (NO) concentration. The DM-FRS system targets $^{14}N^{16}O$ P(19/2)e doublet transition at 1842.946 cm^{-1} (major isotope of NO). The pressure was at 80 Torr.

The numerical modeling is conducted by a zero-dimensional hybrid ZDPlasKin-CHEMKIN model [142]. The discharge voltage measured is used as input to calculate the E/N in the plasma. A plasma-assisted n-dodecane combustion mechanism was developed and validated. The mechanism consists of both plasma and combustion kinetic sub-mechanisms. The combustion sub-mechanism is reduced from Cai's model [143]. The C_0–C_2 sub-mechanism was updated by HP-Mech for accurate modeling of the LTC. The reactions of N and NO_x with fuel and fuel radicals, adapted from Ref. [144]. The plasma mechanism includes electronically excited species of O_2^*, O^*, N_2^*, and N^*, ions such as N_2^+ and O_2^+. The N_2 and O_2 rotationally and vibrationally excited species were also considered to provide slow gas heating. As the n-dodecane pyrolysis and oxidation experiments were conducted at the high diluted conditions and the cross sections of electron-impact n-dodecane dissociation reactions are not available, it was assumed that the fuel was mainly consumed by the electronically excited N_2(A), N_2(B), N_2(a'), N_2(C)) in pyrolysis and also by O(^{1}D) and O(^{1}S) in the oxidation case. Due to the fast collisional relaxation of N_2(B) and N_2(C) to N_2(A) and N_2(a') with N_2, the n-dodecane consumption by N_2^* in the pyrolysis can be simplified by N_2(A) and N_2(a'). Therefore, the reactions of n-dodecane consumption via N_2(A), N_2(a'), O(^{1}D) and O(^{1}S) are listed in Table 5.6. The branching ratios and reaction rates of these reactions were estimated based on fitting with experimental data and sensitivity analysis.

Figure 5.30a shows the comparison of measured and predicted time-dependent CH_4 and C_2H_2 number densities in the pyrolysis condition. Note that the measured temperature evolution was used in the modeling. These species-time histories and the data of the steady-state measurements

TABLE 5.6
Dissociation Reactions of n-Dodecane via N_2(A), N_2(a'), O(^{1}D) and O(^{1}S) Collisions

Excited Species	Dissociation Reactions by Excited Molecules
N_2(A) (6.17–7.8 eV)	$N_2(A)+C_{12}H_{26} \rightarrow N_2+C_{12}H_{25}+H$ $N_2+C_{10}H_{21}+C_2H_5$ $N_2+C_8H_{17}+C_3H_6+CH_3$
	…
N_2(a') (8.4–8.89 eV)	$N_2(a')+C_{12}H_{26} \rightarrow N_2+C_{10}H_{21}+C_2H_4+H$ $N_2+C_{10}H_{21}+CH_3+CH_2$
	…
O(^{1}D)	$O(^1D)+C_{12}H_{26} \rightarrow C_{12}H_{25}+OH$ $C_{10}H_{21}+CH_3+CH_2O$
	…
O(^{1}S)	$O(^1S)+C_{12}H_{26} \rightarrow C_{12}H_{25}+OH$ $C_{10}H_{21}+CH_3+CH_2O$
	…

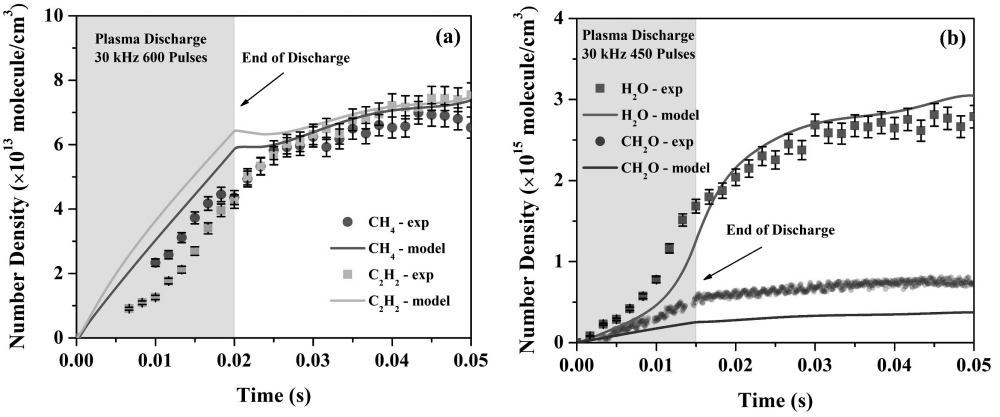

FIGURE 5.30 Time evolution of measured and predicted (a) CH_4 and C_2H_2 for the pyrolysis of 0.01 $C_{12}H_{26}$/0.99N_2 mixture and (b) H_2O and CH_2O for the oxidation of 0.01 $C_{12}H_{26}$/0.19O_2/0.8N_2 mixture.

by GC were used to determine the reaction channels and the branching ratios between N_2(A, a') with fuel (Table 5.6). The developed model well-predicts the major pyrolysis species. Therefore, the time-dependent multispecies diagnostics provided a critical target to estimate the reaction branching ratios and rates in Table 5.6. The path flux analysis showed that n-dodecane was dissociated by N_2(A) (61.4%) and N_2(a') (24%) to produce small hydrocarbon directly or fuel radicals, as well as by H-abstraction reaction (14.6%) to produce H_2 and $C_{12}H_{25}$.

As shown in Figure 5.30b, the model also predicts the time profile of H_2O reasonably well. Up to 90% of H_2O was produced from the $C_{12}H_{26}$+OH reaction. However, like the case of methane oxidation (Figure 5.21), there is an under-prediction for CH_2O, which may result from reactions directly converting hydroperoxy alkyl radicals such as O_2QOOH to CH_2O which were not included in this model.

Comparisons between the measured and predicted speciation in steady-state pyrolysis and oxidation cases of plasma-assisted n-dodecane are shown in Figure 5.31, respectively. In the pyrolysis case, the measured species matched relatively well with the simulation for different discharge frequencies. For oxidation, the primary oxidative products such as H_2O, CH_2O, CO, and CO_2 with high concentrations from the modeling matched reasonably well with the experimental measurements. However, small hydrocarbons were under-predicted. Note that in the oxidation case with a high oxygen concentration and atomic oxygen production, small hydrocarbons produced by the electron-impact dissociation or ionization reactions from n-dodecane may need to be considered appropriately. By estimating the rates of electron-impact reactions with n-dodecane using the similarity rule from pentane and including them in the model, it is seen that the updated model (Figure 5.31b) improved the prediction of the experimental data of small hydrocarbons production. This indicates that the accurate branching ratios and cross sections of electron impact reactions for large hydrocarbons are critical and dedicated measurements and quantum calculation for electron-impact dissociation and ionization reactions are required for future plasma-assisted kinetic studies.

The path flux analysis in Figure 5.32 shows that $C_{12}H_{26}$ consumption by N_2(A, a') and O(^{1}D,^{1}S) accounts for 3.5% and 6.1% of total fuel consumption, and contributes to the production of fuel radicals and CH_2O. N-dodecane consumption by OH and O was the dominant fuel consumption pathways, accounting for 65.3% and 23% of n-dodecane consumption, respectively. The O radical production in plasma promotes the H-abstraction reaction of n-dodecane to form $C_{12}H_{25}$ and OH. It is seen that the production of $C_{12}H_{25}$ leads to the formation of $C_{12}H_{25}O_2$ at low temperature via the addition of O_2 and subsequently to the formation $C_{12}H_{24}$OOH, which becomes a major channel of low-temperature chain-branching (R5.56).

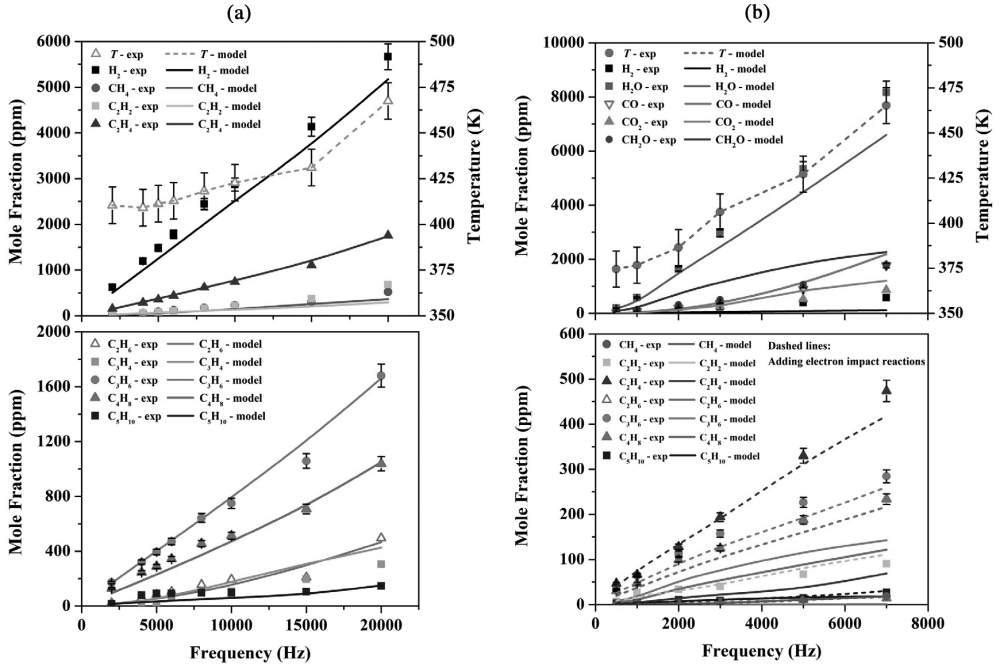

FIGURE 5.31 Comparisons between the measured and predicted species in steady state of plasma-assisted n-dodecane pyrolysis and oxidation cases. (a) Pyrolysis: 0.01 $C_{12}H_{26}$/0.99 N_2. (b) Oxidation: 0.01 $C_{12}H_{26}$/0.19 O_2/0.80 N_2.

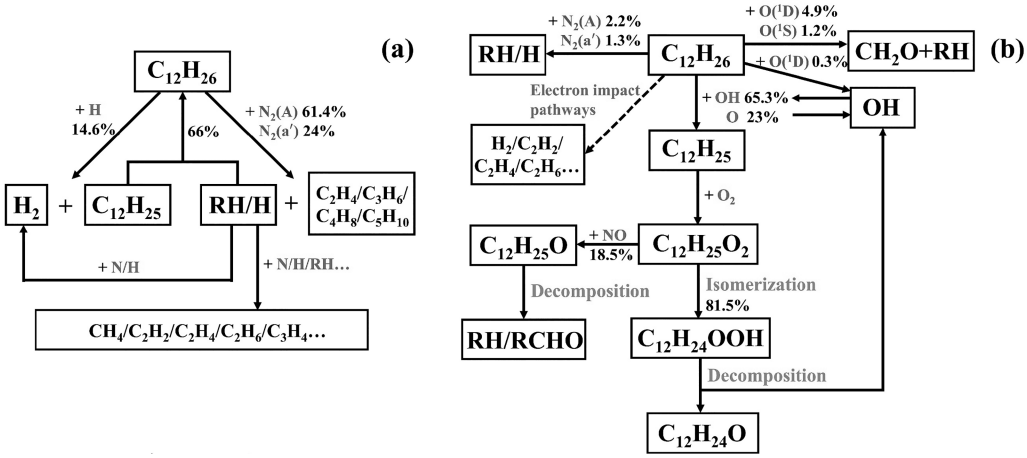

FIGURE 5.32 Path flux of fuel in the time-dependent simulations for (a) the pyrolysis case and (b) the oxidation case.

Therefore, the major plasma-combustion kinetic coupling in plasma-assisted combustion is through the production of small radicals and active intermediate species (Figure 5.33). In summary, for large hydrocarbons and oxygenated fuels, the direct impact dissociation by electron, excited molecules, and ions with fuel molecules in plasma discharge (R5.33'–R5.37') is important and needs to be appropriately considered. However, many cross-sections of electron impact dissociation

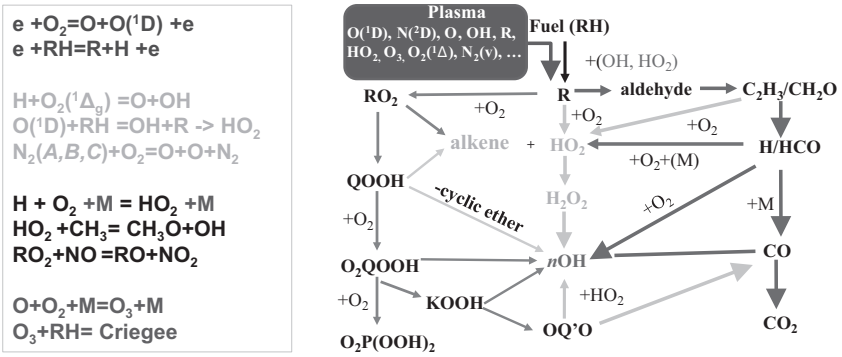

FIGURE 5.33 Schematic of plasma-assisted reaction pathways in affect chain-branching reactions at low, intermediate, and high temperatures, respectively.

TABLE 5.7
Available Electron-Impact Cross-Section Areas for Molecules in Atmosphere and Fuels

Molecules in Atmosphere	Saturated Hydrocarbon	Oxygenates	Isomers
N_2	H_2	CO	
O_2	CH_4	CH_3OH	
CO_2	C_2H_6	C_2H_5OH	
H_2O	C_3H_8	CH_3OCH_3	i-C_3H_8
O_3	C_4H_{10}		i-C_4H_{10}
Ar	C_5H_{12}		i-C_5H_{12}
N_2O			

reactions for large hydrocarbons and oxygenated fuels are not available. Table 5.7 shows the availability of electron-impact reaction cross-section areas for molecules in atmosphere, hydrocarbons, and oxygenates. It is seen that cross-section area data for many large hydrocarbons and oxygenates are still missing. Moreover, the reaction cross-section areas and rate constants for dissociation and oxidation of fuel molecules by excited molecules like N_2^*, O_2^*, O^*, N^* and nitrogen, oxygen, fuel ions, O_3, and NO_x are also not available.

$$e + RH \rightarrow e + R + H \quad \text{(R5.33a')}$$

$$e + RH \rightarrow e + R' + H + CH_3 \quad \text{(R5.33b')}$$

$$e + RH \rightarrow 2e + R^+ + H \quad \text{(R5.33c')}$$

$$N_2^+ + RH \rightarrow N_2 + R + H \quad \text{(R5.34a')}$$

$$N_2^+ + RH \rightarrow N_2 + R + R' \quad \text{(R5.34b')}$$

$$O_2^* + RH \rightarrow RO + R'O \quad \text{(R5.35a')}$$

$$O_2^* + RH \rightarrow R + R'O_2 \quad \text{(R5.35b')}$$

$$O^* + RH \rightarrow R + OH \quad \text{(R5.36a')}$$

$$O^* + RH \rightarrow R'O + R''H \quad \text{(R5.36b')}$$

$$N_2^+ + RH \rightarrow R^+ + R' + N_2 \quad \text{(R5.37')}$$

5.3 IMPACT OF O(¹D), NO_x, AND OZONE PRODUCTION IN PLASMA ON COMBUSTION KINETICS

5.3.1 O(¹D) Reactions with Saturated and Unsaturated Hydrocarbons and Oxygenates

The O(¹D) + fuel reactions are among the key reactions in plasma-assisted combustion, atmospheric chemistry, and chemical reforming. Because of the high internal energy of O(¹D), these reactions are very fast and have many possible reaction channels via H-abstraction and direct O-atom insertions. The resulting products have very different reactivities, thus affecting the reaction process significantly. Therefore, it is important to determine the branching ratios of O(¹D) + fuel reactions. With the recent progress in quantum chemistry calculations and *in situ* laser diagnostics, some progress has been made in quantifying O(¹D) reactions with hydrocarbons and oxygenated fuels [91,92,145–147]. In the sections below, we will summarize a few direct measurements and quantum chemistry calculations of O(¹D) reactions with CH_4, C_2H_2, alcohol, and ether, respectively.

5.3.1.1 O(¹D) + CH_4 Reactions

The reaction of O(¹D) with methane has several channels (Table 5.8). A recent quantum chemistry calculation at multireference configuration interaction MRCI+Q/CBS level with the zero-point energy correction obtained from CAS(10,10)/cc-pVDZ results show that the major reaction channels of O(¹D) + CH_4 are R5.25a'–R5.25f'. Equation R5.25b' is a dominant channel. The predicted branching ratios for OH and H production are, respectively, 0.73 and 0.18. Note that H radical is

TABLE 5.8
Reaction Channels of O(¹D) + CH_4 Reactions and Computed Branching Ratios [146]

O(¹D) + CH_4 → reactions	Branching Ratio	R5.25′
$H_2 + CH_2O$	0.0252	R5.25a'
$OH + CH_3$	0.7299	R5.25b'
$CH_2 + H_2O$	0.0648	R5.25c'
$H + CH_3O$	0.1178	R5.25d'
$H + CH_2OH$	0.0548	R5.25e'
$H + H + CH_2O$	0.0075	R5.25f'

more reactive than OH in many plasma-assisted combustion systems. As such, although reactions R5.25d' and R5.25f' have small product ratios but the production of H and other radicals render these reaction channels ineligible.

5.3.1.2 $O(^1D) + C_2H_2$ Reactions

For $O(^1D)$ reactions with unsaturated hydrocarbons, the rate constants and the branching ratios are not well known. Recently, by using highly selective mid-infrared Faraday rotation spectroscopy (FRS) (Figure 9.22) [140,141,148] with a digitally balanced detection scheme (Figure 9.23) to probe the time histories of $O(^1D)$, HO_2, OH, and H_2O in the reaction of $O(^1D)$ with acetylene, the branching ratios of $O(^1D) + C_2H_2$ reactions were determined in Table 5.9.

The experimental setup of the UV photolysis reactor integrated with FRS and LAS is shown in Figure 5.34 [92]. $O(^1D)$ was generated by UV photolysis of O_3 at 266 nm. To determine the important kinetic information, time-dependent measurements of OH, HO_2, C_2H_2, O_3, and H_2O were carried out by FRS and LAS in $C_2H_2/O_2/O_3$/He mixtures. By comparing the kinetic model simulations with the time-dependent experimental measurements of O_3, OH, and HO_2, the important chain-branching ratios for the various channels of reaction between $O(^1D)$ and C_2H_2 were determined.

TABLE 5.9
Reaction Channels of $O(^1D) + C_2H_2$ Reactions and Computed Branching Ratios [92]

$O(^1D) + C_2H_2 \rightarrow$	Branching Ratio	R5.38′
C_2H_2O	0.56	R5.38a'
HCCO+H	0.22	R5.38b'
CH_2+CO	0.22	R5.38c'
C_2H+OH	0	R5.38d'

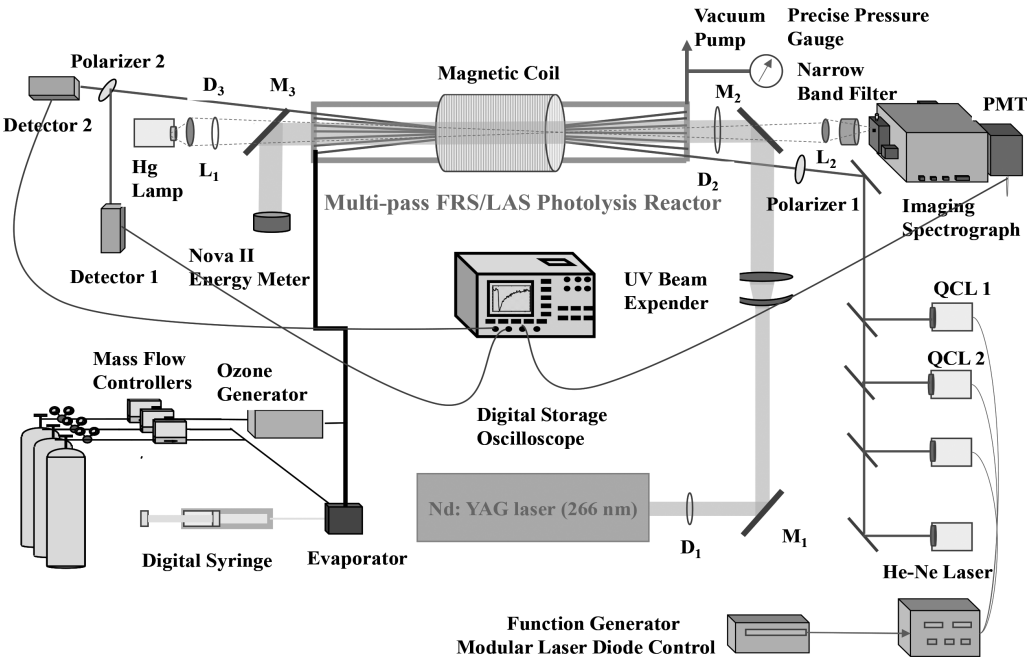

FIGURE 5.34 Schematic of experimental setup of the UV photolysis reactor integrated with Faraday rotation spectroscopy (FRS) and LAS [92].

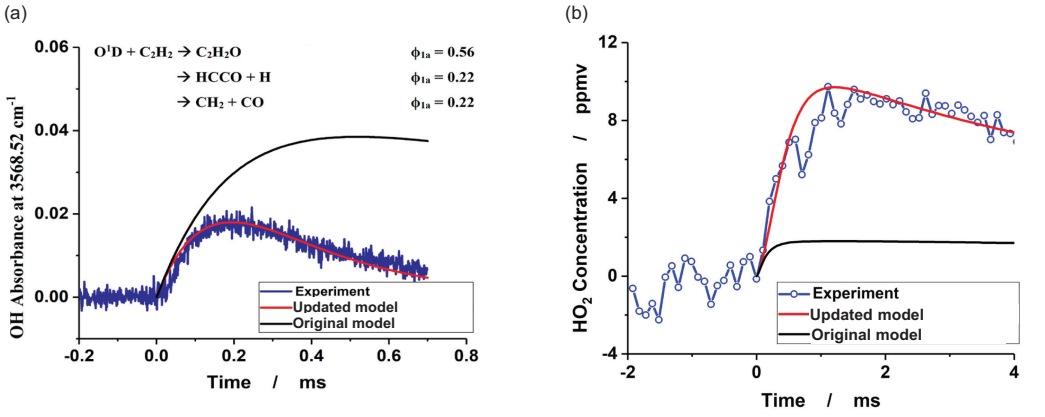

FIGURE 5.35 Comparison of the experimental data and simulation based on HP-Mech [92] with (updated model) and without (original model) the new rates of R38'. Experimental conditions: 60 Torr and 296 K in a gas mixture of $C_2H_2/O_2/O_3$/He. $[C_2H_2]=1.32\times10^{16}$, $[O_2]=4.94\times10^{15}$ and $[O_3]=2.95\times10^{14}$ molecules/cm. (a) The time-resolved measurement of OH radicals. (b) The time-resolved measurement of HO_2 radicals [92].

Figure 5.35a shows the measured and modeled OH radical production time history. There is a good agreement between simulation using an updated mechanism and the branching ratio of R5.38'. It is seen that right after the laser photolysis, OH was produced via $O(^1D)+C_2H_2$ reactions. By fitting the time history of the experimental data, the branching ratio of R5.38' for OH production was estimated. The derived branching ratios of channels R5.38a', R5.38b', and R5.38c' are 56%, 22%, and 22%, respectively. Time-resolved measurements of HO_2 formation from $O(^1D)+C_2H_2$ reactions are shown in Figure 5.35b. The reaction path flux analysis indicated that a missing reaction channel of

$$C_2H_2OH+O_2\rightarrow HO_2+HCCOH\quad\left(1\times10^{12}\ \text{cm}^3/\text{mole s}\right)\tag{R5.67}$$

needs to be added to HP-Mech. The updated model with inclusion of R5.67 significantly improved the prediction. As shown in Table 5.9, unlike saturated hydrocarbons, for $O(^1D)$ reactions with unsaturated hydrocarbons, the H-abstraction channel to form OH may not necessarily be the main channel.

5.3.1.3 $O(^1D)$ + alcohol Reactions

By using the same experimental setup in Figure 5.35, the $O(^1D)$ reactions with methanol and ethanol were also experimentally investigated. For example, Figure 5.36 shows the experimental measurement of OH production in $O(^1D)+CH_3OH$ reaction and the model prediction [91,149]. The measured branching ratios and the reaction rate of $O(^1D)+CH_3OH$ are shown in Table 5.10 and Figure 5.36. The present experimental data are consistent with the previous work of Huang et al. [149]. A similar experiment of ethanol was also conducted for $O(^1D)+C_2H_5OH$ [91]. The measured branching ratios for four major reaction pathways are listed in Table 5.10. It is seen that Reaction R5.40a' and R5.40d' are the major reaction channels. Therefore, both $O(^1D)+CH_3OH$ and $O(^1D)+C_2H_5OH$ reaction kinetics show that $O(^1D)$ + fuel reactions are all multi-channeled and much more complicated than O + fuel reactions on the ground state. Care is needed in developing plasma-assisted combustion models for $O(^1D)$ reactions.

5.3.1.4 $O(^1D)+CH_3OCH_3$ Reactions

Recently Zhong et al. [150] experimentally and theoretically integrated the complex multichannel reaction dynamics and determined the total reaction rate and branching ratio of this reaction by using *in situ* laser spectroscopy and ab initio quantum chemistry theory. The computationally determined total reaction rate at 300 K and 30 Torr is $k=2.98\times10^{-10}$ cm^3/molecule s. The branching ratios

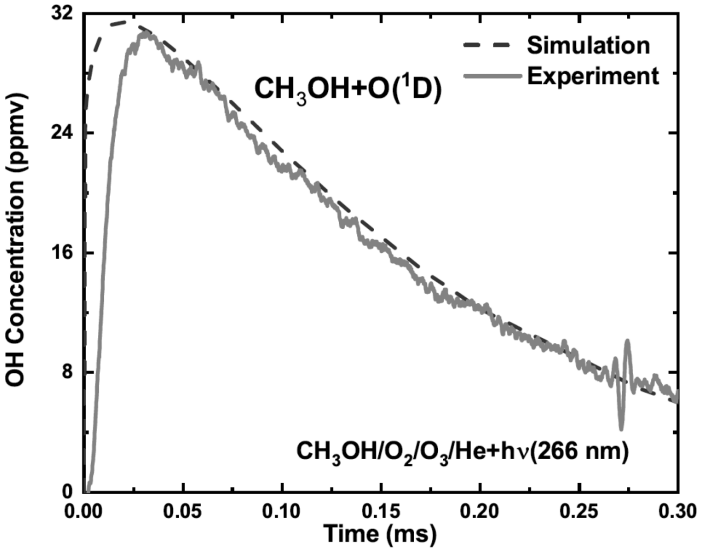

FIGURE 5.36 Comparison of measured and predicted OH production time history in $O(^1D)+CH_3OH$ reaction system at 296 K and 150 Torr. The total reaction rate is $k_{CH_3OH+O(^1D)} = (3.0 \pm 0.3) \times 10^{14}$ cm^3/moles [91].

TABLE 5.10
Measured Branching Ratios of $O(^1D)$ Reactions with Methanol and Ethanol [91]

$O(^1D)+CH_3OH \rightarrow$	Branching Ratio	R5.39′
CH_2OH+OH	0.55	R5.39a’
$HOCHO+2H$	0.45	R5.39b’
$O(^1D)+C_2H_5OH \rightarrow$	**Branching Ratio**	**R5.40’**
$CH_3CHOH+OH$	0.46	R5.40a’
CH_2CH_2OH+OH	$0.12-x$	R5.40b’
CH_3CH_2O+OH	x	R5.40c’
CH_3O+CH_2OH	0.41	R5.40d’

TABLE 5.11
Measured Branching Ratios of $O(^1D)$ Reactions with Dimethyl Ether [150]

$O(^1D)+CH_3OCH_3 \rightarrow$	Branching Ratio 30 Torr	Branching Ratio 60 Torr	R5.41′
CH_3OCH_2+OH	0.03	0.06	R5.41a’
CH_3O+CH_3O	0.90	0.76	R5.41b’
CH_3O+CH_2OH	0.07	0.18	R5.41c’

for reactions R5.41’ in Table 5.11 are, respectively, 0.03, 0.90, and 0.07. Clearly, R5.41b’ to form two CH_3O molecules is the dominant one. At 60 Torr and 300 K, the predicted reaction rate increases to $k = 4.41 \times 10^{-10}$ cm^3/molecule s and the experimentally fitted branching ratios become 0.06. 0.76, and 0.18, respectively. Therefore, the branching ratio is pressure-dependent.

5.3.2 Plasma-Produced NO_x and the Impact on Combustion Kinetics

Plasma discharge creates a lot of excited nitrogen and nitrogen atoms which lead to the formation of NO_x (e.g. R5.32'). The resulting NO_x has a significant impact on combustion kinetics [70,144,151–153]. In addition, the NO_x effect on combustion kinetics is temperature and fuel-dependent. For example, Figure 5.37 shows the measured NO production in plasma-assisted n-dodecane oxidation in the experiment of Figure 5.31. It is seen that for plasma discharge without fuel (n-dodecane), NO production monotonically increased with the discharge frequency (plasma power). However, with n-dodecane addition, NO production dramatically decreased. This result may give readers a misunderstanding that plasma-assisted combustion will decrease NO production. The real answer is that it may and may not.

To understand the impact of plasma-generated NO_x on combustion kinetics and the kinetic coupling between NO_x chemistry with combustion chemistry, Zhao et al. [70,144,153] conducted kinetic studies of NO_x addition on the oxidation of large hydrocarbons such as n-pentane and n-dodecane. The mutual oxidation of n-pentane/n-dodecane and NO_x (NO and NO_2) at 500–1,000 K were studied at fuel lean and rich conditions by using an atmospheric-pressure jet-stirred reactor (JSR). Multispecies measurements were conducted by using an electron-impact molecular beam mass spectrometer (EI-MBMS), a micro-gas chromatograph (μ-GC), and a mid-IR dual-modulation Faraday rotation spectrometer (DM-FRS). The results (Figure 5.38) show that at both lean and rich conditions, NO_x addition has different sensitization characteristics on fuel oxidation in three different temperature windows. For n-pentane, between 550 and 650 K (region 1 in Figure 5.38), NO addition inhibits low-temperature oxidation. With an increase of temperature to the NTC region (650–750 K) (region 2 in Figure 5.38), NO addition suppresses the NTC behavior at the fuel lean condition. In the intermediate and high-temperature region (750–1,000 K) (region 3 in Figure 5.38), fuel oxidation is accelerated with NO addition. Kinetic models predicted reasonably well the temperature-dependent NO/NO_2 sensitization effect on fuel oxidation [144,153]. The results also show that although NO_2 addition in n-pentane has similar effects to NO at many conditions due to fast NO and NO_2 interconversion at higher temperature, it affects low-temperature oxidation somewhat differently. When NO_2/NO interconversion is slow at low temperature, NO_2 is relatively inert while

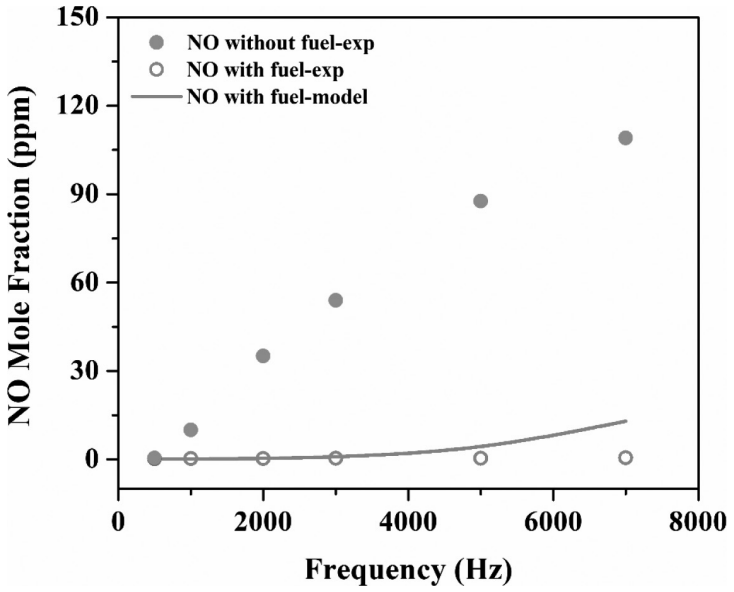

FIGURE 5.37 NO measurements with the increase of plasma pulse frequencies for normal air ($0.20O_2/0.80N_2$) and $0.01C_{12}H_{26}/0.19O_2/0.80N_2$ mixture [108].

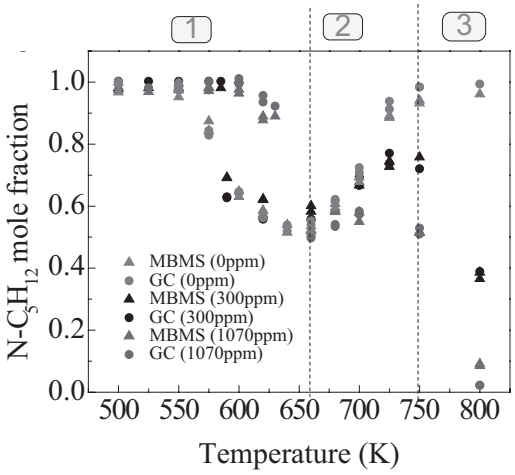

FIGURE 5.38 Temperature evolution of the mole fraction of n-pentane at the fuel lean conditions ($\varphi = 0.5$) with different amounts of NO additions (0, 300, and 1,070 ppm) [144].

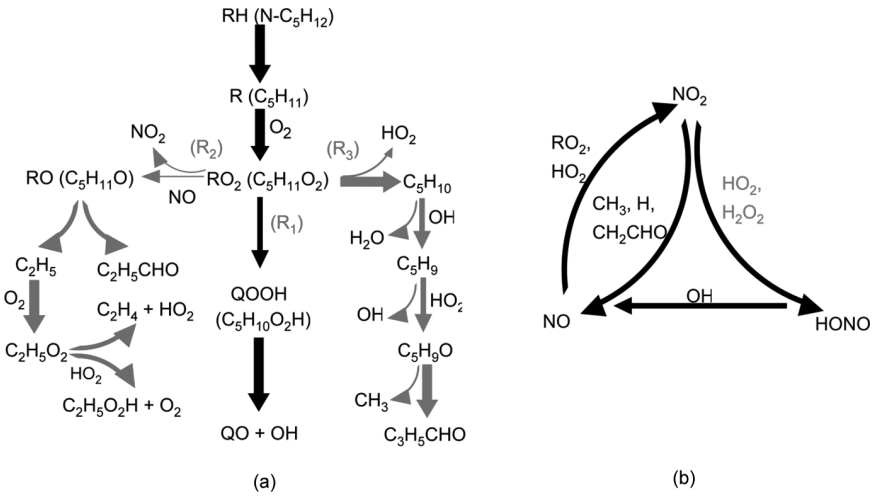

FIGURE 5.39 Kinetic coupling between NO_x chemistry at low (a) and intermediate temperature (b) fuel oxidation chemistry.

NO can strongly promote or inhibit fuel oxidation. In addition, NO addition delays the onset temperature of n-pentane low-temperature oxidation and strongly inhibits the NTC effect, while NO_2 has little effect on the onset temperature and weaker impact on NTC.

The kinetic coupling between NO_x chemistry, low-temperature combustion chemistry, and intermediate temperature HO_2 chemistry is schematically shown in Figure 5.39. In the low-temperature oxidation region, there are two reaction channels for NO to affect OH radical production, respectively, via RO_2 consumption (R5.68) and OH radical quenching (R5.69) to slow down the low-temperature reactivity,

$$RO_2 = QOOH \tag{R5.49a}$$

$$RO_2 = R' + HO_2 \tag{R5.49b}$$

$$RO_2 + NO = RO + NO_2 \quad \text{(R5.68)}$$

$$NO + OH + M = HONO + M \quad \text{(R5.69)}$$

Since R5.49a and R5.56 are the major low-temperature chain-branching reactions via RO_2, the RO_2 radical quenching via R5.68 will slow down OH radical production. Moreover, reaction R5.69 will further terminate OH radicals at low temperature. Therefore, the low-temperature oxidation (Figure 5.38) is inhibited and shifted to a higher temperature.

In the NTC region, the kinetic coupling between NO_x chemistry and HO_2 chemistry will accelerate radical production and suppress the NTC effects due to RO_2 and QOOH decomposition via R5.48 and R5.50, thus enhancing fuel oxidation (Figure 5.38). As shown in the reactions listed below, HO_2 starts to react with NO (R5.41) and CH_3 (R5.15) at elevated temperature to produce OH and NO_2. Then, HO_2 will react with NO_2 to form HONO and OH via reaction R5.70 and R5.69b. In addition, the resulting NO_2 from R5.41 will further react with CH_3 and CH_2O to form a catalytic reaction pathway for OH production (R5.41, R5.71, and R5.72). As such, one can see from Figure 5.38 that NO_x addition into n-heptane will significantly enhance the intermediate temperature fuel oxidation and suppress the NTC effect. Therefore, plasma-produced NO_x will dramatically impact fuel oxidation chemistry and such effects are temperature- and fuel-dependent. The plasma-produced NO_x coupling effect needs to be appropriately incorporated into plasma-assisted combustion chemistry when involving nitrogen containing species.

$$HO_2 + NO = OH + NO_2 \quad \text{(R5.41)}$$

$$NO_2 + HO_2 = HONO + O_2 \quad \text{(R5.70)}$$

$$HONO + M = OH + NO + M \quad \text{(R5.69b)}$$

$$CH_3 + HO_2 = CH_3O + OH \quad \text{(R5.15)}$$

$$NO_2 + CH_3 = CH_3O + NO \quad \text{(R5.71)}$$

$$CH_2O + NO_2 = HCO + HONO \quad \text{(R5.72)}$$

5.3.3 Plasma-Produced, Ozone-Assisted Combustion Kinetics

Ozone is one of the key species produced in nonequilibrium plasma involving oxygen. In addition, it is a long-lived species in dry air at temperatures below 400 K (approximately 1,500 min at room temperature). It can be efficiently and economically produced at high pressure using DBD discharge in industry [154]. It is also an important species in atmospheric chemistry [155]. The interest in ozone effects on combustion can be traced back to the 1950s [156]. Since then, ozone effects on chemistry [96,97,139,157–161], ignition [162,163], hot flames [139,156–158,163–168], cool flames and warm flames [78,79,158,166,169–172], detonation [95,165], and engines [162,163,173] have been extensively explored. The studies showed that ozone can promote extreme low-temperature oxidation [96,174–176], ignition [162,163], cool flames [157,158,167], and detonation [95,165].

There are several ways (Table 5.12) that ozone will affect combustion kinetics at different temperatures and fuel molecule structures.

The first pathway of ozone impact on combustion is producing radicals via thermal decomposition or H-abstraction (R5.73–R5.74). Zhao et al. [139] measured ozone decomposition in a flow reactor with flow residence time approximately at 0.5 s under different temperatures. Figure 5.40 shows that ozone started to decompose around 410 K and the decomposition ratio reached 50% at 500 K. Therefore, ozone can produce O radicals via thermal decomposition at a temperature where most fuels do not have any reactivity. As such, the radical production via ozone decomposition at

TABLE 5.12
Low-Temperature Ozone Termination and Radical Production and Propagation Reactions

Ozone Reactions	Impact on Combustion	
	Radical Production Reactions	
$O_3 + M = O_2 + O + M$	Producing O radicals below 500 K	R5.73
$O + RH = R + OH$	OH production from saturated hydrocarbons/oxygenates	R5.74
	Radical Propagation Reactions	
$O_3 + H = O_2 + OH$	Changing chain-branching reaction rate	R5.75
$O_3 + OH = O_2 + HO_2$	Reducing low-temperature reactivity	R5.76
$O_3 + HO_2 = 2O_2 + OH$	Changing low-temperature reactivity	R5.77
	Ozonolysis Reactions with Unsaturated Hydrocarbons and Oxygenates	
$O_3 + \text{alkene} \rightarrow \text{POZ} \rightarrow \text{Criegee}$		
$O_3 + C_2H_4 = CH_2O + CH_2OO^*$	Rapid radical production at low temperature	R5.78
	Quenching Reactions	
$O_3 + O = O_2 + O_2$	Losing chemical reactivity for heating	R5.79
$NO + O_3 = NO_2 + O_2$	Losing chemical reactivity but modifying NO_x chemistry	R5.80
$SO_2 + O_3 = SO_3 + O_2$	Loss of chemical reactivity but enabling SO_2 capture	R5.81

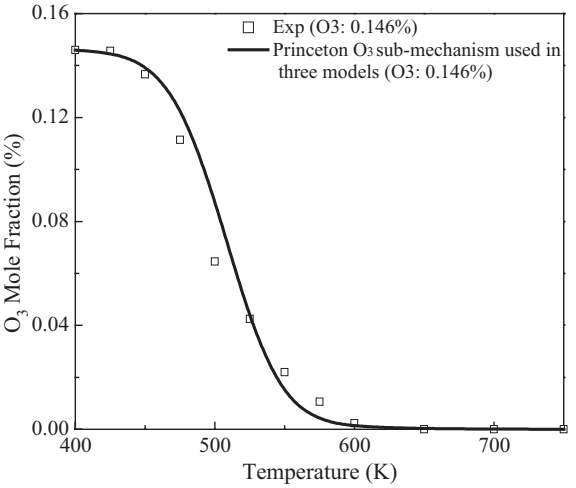

FIGURE 5.40 Measured and predicted O_3 mole fraction profiles with varied temperatures in a flow reactor O_3 decomposition experiment with flow residence time around 0.5 s [139].

extremely low temperature can initiate low-temperature fuel oxidation at a temperature outside the conventional fuel LTC window.

Recent experiments by Zhao et al. [139] and Rousso et al. [175] studied the ozone-initiated low-temperature oxidation of dimethyl ether and methyl hexanoate, respectively. Both studies reported that ozone addition into these oxygenated fuels induced low-temperature fuel oxidation at temperatures below 500 K. Figure 5.41 shows the ozone depletion in the absence of other reactants and the modeled atomic O concentration as well as alkyl hydroperoxides distribution of ozone-assisted methyl hexanoate (MHX) oxidation in a JSR [175]. It is clear from this figure that about 80% of O_3 were decomposed and consumed at the extreme low-temperature combustion (ELTC) region centered at 500 K. Simultaneously, the model predicted that the O concentration rose due to the thermal decomposition (R5.73). At the same time, as indicated by methyl hydroperoxide CH_4O_2 and methyl-formate $C_2H_4O_2$ concentrations, LTC occurred in the ELTC region. In the non-ozone case, the dashed red line shows zero CH_4O_2 signal. Therefore, the fuel oxidation at the ELTC region was induced by ozone-sensitized LTC, which promotes radical production via R5.74. Quantum chemistry simulation showed that the reaction rate of methyl hexanoate with O (R5.74) is considerably higher than that of dimethyl ether. Once the fuel radical was formed by R5.73 and R5.74, the LTC chemistry pathway (R5.56) would be enhanced and resulting in the new reaction zone at ELTC. The resulting temperature-dependent profiles of the hydroperoxide species (including the keto-hydroperoxide) were measured and shown in Figure 5.42. It is seen that the hydroperoxide concentrations in the ELTC region are higher than that in the LTC region. This may be because temperatures were not sufficiently high enough for the keto-hydroperoxide to dissociate as in the normal LTC region.

The second reaction pathway of ozone radical propagation reactions in Table 5.12 may only occur during *in situ* plasma discharge because ozone does not exist at high temperature at which H and OH are created. With *in situ* plasma discharge which creates high concentrations (10–100 ppm level) of H/OH/HO_2 and 0.1%–10% of ozone at room temperature, these radical propagation reactions will occur. This reaction pathway needs to be included in plasma-assisted combustion and fuel reforming.

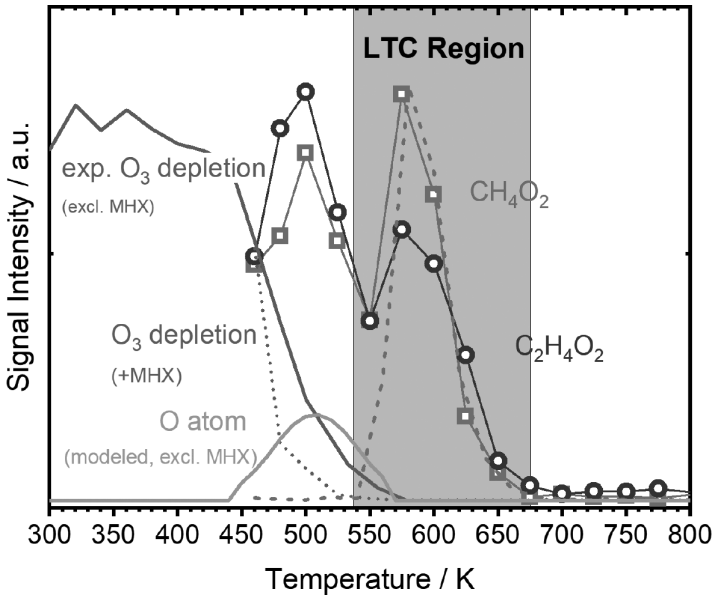

FIGURE 5.41 Temperature profiles of ozone depletion (solid green line), ozone depletion in the presence of MHX (dotted green line), modeled O-atom concentration (O_3 only in the absence of the reactant MHX) and observed double-peak structures of methyl hydroperoxide CH_4O_2 and $C_2H_4O_2$ profiles. The dashed line for CH_4O_2 represents data from the non-ozone case.

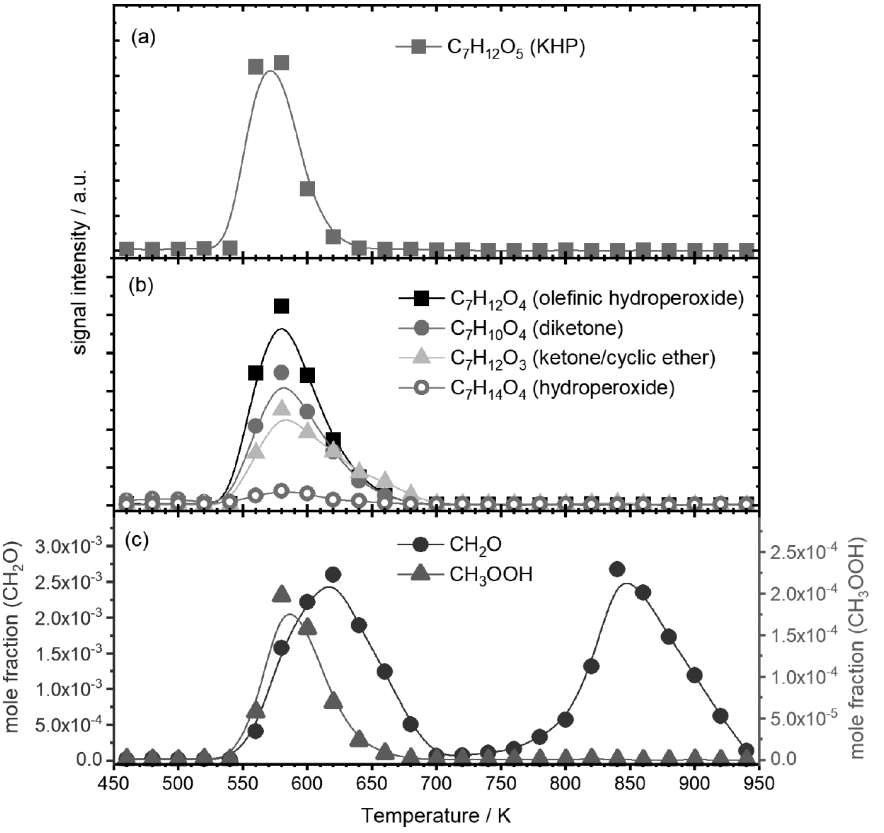

FIGURE 5.42 Temperature dependence of panel (a) keto-hydroperoxides (KHPs), (b) olefinic hydroperoxides, diketones, ketones/cyclic ethers, and hydroperoxides, and (c) methyl hydroperoxide and formaldehyde follow the trends typical for LTC behavior. This non-ozone data was taken using electron ionization (EI).

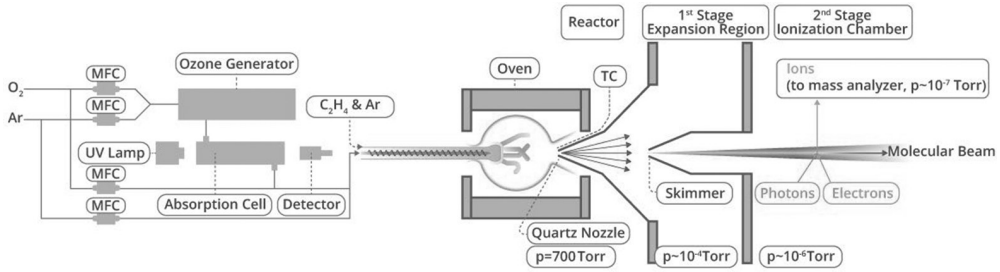

FIGURE 5.43 Experimental Setup for the JSR. The ozone detection cell is just upstream of the JSR. The stages of the MBMS sampling from the JSR are shown on the right.

The third reaction pathway is the ozonolysis reaction [174,177] in which the unsaturated hydrocarbon bonds are cleaved with ozone to form reactive products such as the criegee intermediate. Recent reviews of the chemistry of criegee intermediates can be found in Refs. [178,179], Rousso et al. [174], and Sun et al. [176] studied the low-temperature reaction kinetics of ozone reaction with ethylene. Figure 5.43 shows the experimental apparatus for the study of ozone-assisted ethylene oxidation in a heated JSR [174].

For ethylene, the ozonolysis reaction pathway is schematically shown in Figure 5.44 following the studies of Refs. [180,181]. The ozonolysis initially forms a chemically activated primary ozonide

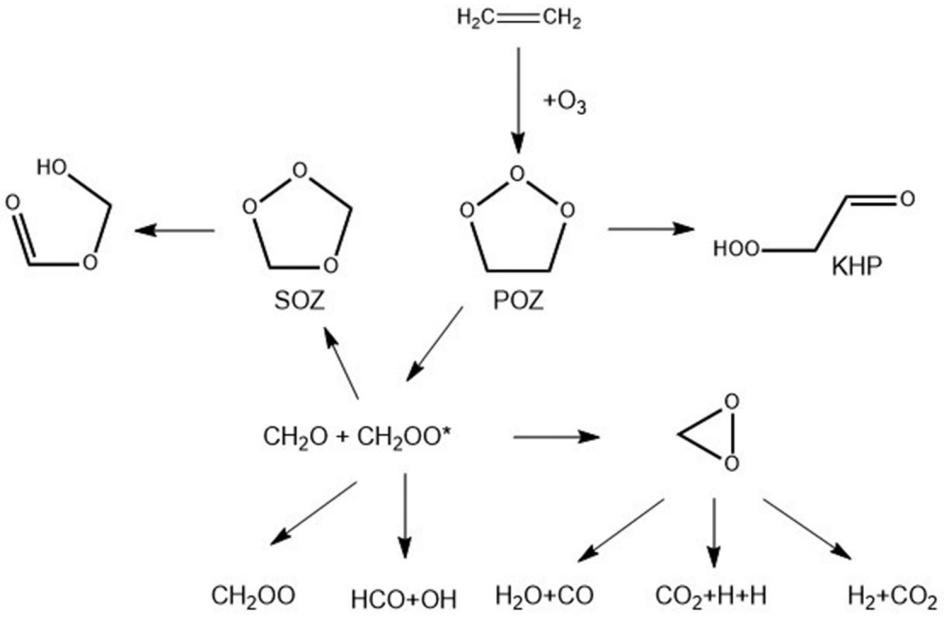

FIGURE 5.44 Ethylene ozonolysis reaction pathway with major intermediate species.

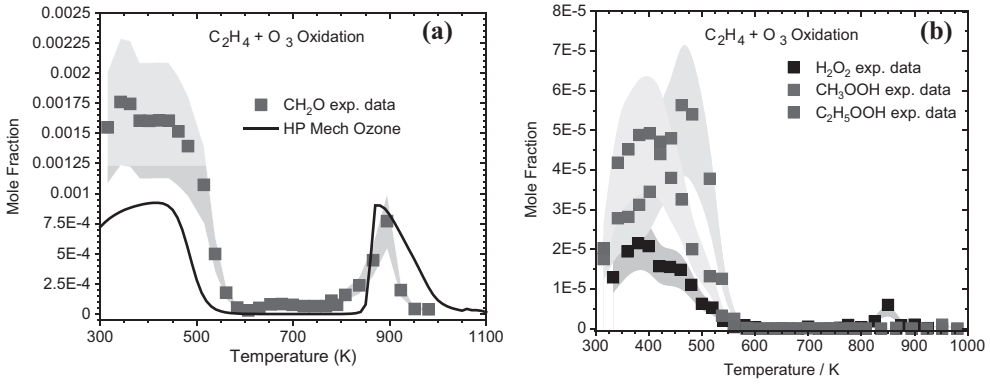

FIGURE 5.45 Species dependence on temperature measured and predicted in ozone-assisted reaction with ethylene in a JSR. (a) CH_2O mole fraction, (b) measurements of the H_2O_2, CH_3OOH, and C_2H_5OOH concentrations.

(POZ) and then quickly dissociates in the formation of formaldehyde and CH_2OO^*, the simplest criegee intermediate, which subsequently stabilizes or further decomposes to radicals.

The ozonolysis reaction between ozone and ethylene occurs at room temperature. Rate coefficients for many of these reactions have been experimentally determined or calculated between 293 and 300 K and 1 atm, with branching fractions of ~37% (CI stabilization), 15% (HCO+OH), 30% (H_2O+CO), <1% (CO_{2+}H+H), and 18% ($H_{2+}CO_2$) [180]. However, experimental studies of ozonolysis reactions at elevated temperatures have not been well investigated.

Figure 5.45 shows the measured and simulated temperature dependence of intermediate species formation in ozone-ethylene reactions in a JSR (Figure 5.43). It is clearly seen that CH_2O and peroxide species were formed between room temperature and 575 K due to the ozonolysis reactions. Above 575 K, ozone will decompose so quickly that the ozonolysis reaction is suppressed and only the ozone decomposition reaction proceeds which led to very low reactivity, because ethylene does

not have LTC under atmospheric conditions. It is seen that only very low reactivity was observed until the temperature reaches close to 900 K at which the HO_2 chemistry starts to oxidize ethylene and form CH_2O and other peroxide species.

Therefore, in this chapter, we summarized the major reaction pathways of several important fuels including H_2, CH_4, ammonia, and large hydrocarbons and oxygenated fuels. We discussed the rate-limiting chain-initiation, branching, propagation, and termination reactions of these fuel oxidations. Then, we introduced the key elementary reactions in plasma and production of active radicals. The key chain-branching reactions, respectively, at low, intermediate and high temperatures by R5.56, R5.5, and R5.3 are discussed. We demonstrated that plasma-generated key active species and intermediate species as well as products such as NO_x and ozone can promote or inhibit low-temperature combustion. The kinetic impacts of plasma-generated species on combustion strongly depend on temperature and fuel molecule structures. More future research is needed to develop predictive plasma chemistry for combustion and chemical reforming.

In Chapter 6, we will discuss how the plasma-enhanced new reaction pathways, LTC, and ELTC will impact ignition, flame speeds, burning limit, flame regimes, the minimum ignition energy, and detonation.

REFERENCES

1. Wang, Z., et al., Methanol oxidation up to 100 atm in a supercritical pressure jet-stirred reactor. *Proceedings of the Combustion Institute,* 2022. **39**: pp. 1–9.
2. Law, C.K., *Combustion Physics*. 2010: Cambridge University Press.
3. Ruscic, B., Active thermochemical tables: Sequential bond dissociation enthalpies of methane, ethane, and methanol and the related thermochemistry. *The Journal of Physical Chemistry A*, 2015. **119**(28): pp. 7810–7837.
4. Zhao, H., et al., Studies of low and intermediate temperature oxidation of propane up to 100 atm in a supercritical-pressure Jet-Stirred reactor. *Proceedings of the Combustion Institute,* 2023. **39**: pp. 2715–2723.
5. Kobayashi, H., et al., Science and technology of ammonia combustion. *Proceedings of the Combustion Institute,* 2019. **37**(1): pp. 109–133.
6. Song, Y., et al., Ammonia oxidation at high pressure and intermediate temperatures. *Fuel*, 2016. **181**: pp. 358–365.
7. Sullivan, N., et al., Ammonia conversion and NO_x formation in laminar coflowing nonpremixed methane-air flames. *Combustion and Flame*, 2002. **131**(3): pp. 285–298.
8. Glarborg, P., et al., Modeling nitrogen chemistry in combustion. *Progress in Energy and Combustion Science*, 2018. **67**: pp. 31–68.
9. Miller, J.A., et al., Kinetic modeling of the oxidation of ammonia in flames. *Combustion Science and Technology*, 1983. **34**(1–6): pp. 149–176.
10. Li, J., et al., Study on using hydrogen and ammonia as fuels: Combustion characteristics and NO_x formation. *International Journal of Energy Research*, 2014. **38**(9): pp. 1214–1223.
11. Ichikawa, A., et al., Laminar burning velocity and Markstein length of ammonia/hydrogen/air premixed flames at elevated pressures. *International Journal of Hydrogen Energy*, 2015. **40**(30): pp. 9570–9578.
12. Han, X., et al., Experimental and kinetic modeling study of laminar burning velocities of NH_3/air, NH_3/H_2/air, NH_3/CO/air and NH_3/CH_4/air premixed flames. *Combustion and Flame*, 2019. **206**: pp. 214–226.
13. Wang, S., et al., Experimental study and kinetic analysis of the laminar burning velocity of NH_3/syngas/air, NH_3/CO/air and NH_3/H_2/air premixed flames at elevated pressures. *Combustion and Flame*, 2020. **221**: pp. 270–287.
14. Mei, B., et al., Enhancement of ammonia combustion with partial fuel cracking strategy: Laminar flame propagation and kinetic modeling investigation of NH_3/H_2/N_2/air mixtures up to 10 atm. *Combustion and Flame*, 2021. **231**: p. 111472.
15. Lee, J.H., et al., Studies on properties of laminar premixed hydrogen-added ammonia/air flames for hydrogen production. *International Journal of Hydrogen Energy*, 2010. **35**(3): pp. 1054–1064.
16. Lee, J.H., S.I. Lee, and O.C. Kwon, Effects of ammonia substitution on hydrogen/air flame propagation and emissions. *International Journal of Hydrogen Energy*, 2010. **35**(20): pp. 11332–11341.

17. Kumar, P. and T.R. Meyer, Experimental and modeling study of chemical-kinetics mechanisms for H_2–NH_3–air mixtures in laminar premixed jet flames. *Fuel*, 2013. **108**: pp. 166–176.
18. Lesmana, H., et al., Experimental and kinetic modelling studies of laminar flame speed in mixtures of partially dissociated NH_3 in air. *Fuel*, 2020. **278**: p. 118428.
19. Lhuillier, C., et al., Experimental investigation on laminar burning velocities of ammonia/hydrogen/air mixtures at elevated temperatures. *Fuel*, 2020. **263**: p. 116653.
20. Lesmana, H., et al., Experimental and kinetic modelling studies of flammability limits of partially dissociated NH_3 and air mixtures. *Proceedings of the Combustion Institute,* 2021. **38**(2): pp. 2023–2030.
21. Osipova, K.N., O.P. Korobeinichev, and A.G. Shmakov, Chemical structure and laminar burning velocity of atmospheric pressure premixed ammonia/hydrogen flames. *International Journal of Hydrogen Energy*, 2021. **46**(80): pp. 39942–39954.
22. Shrestha, K.P., et al., An experimental and modeling study of ammonia with enriched oxygen content and ammonia/hydrogen laminar flame speed at elevated pressure and temperature. *Proceedings of the Combustion Institute,* 2021. **38**(2): pp. 2163–2174.
23. Wang, N., et al., Laminar burning characteristics of ammonia/hydrogen/air mixtures with laser ignition. *International Journal of Hydrogen Energy*, 2021. **46**(62): pp. 31879–31893.
24. Alfazazi, A., et al., Counterflow flame extinction of ammonia and its blends with hydrogen and C1-C3 hydrocarbons. *Applications in Energy and Combustion Science*, 2022. **12**: p. 100099.
25. Gotama, G.J., et al., Measurement of the laminar burning velocity and kinetics study of the importance of the hydrogen recovery mechanism of ammonia/hydrogen/air premixed flames. *Combustion and Flame*, 2022. **236**: p. 111753.
26. Han, X., et al., Uniqueness and similarity in flame propagation of pre-dissociated NH_3+air and NH_3+H_2+air mixtures: An experimental and modelling study. *Fuel*, 2022. **327**: p. 125159.
27. Hayakawa, A., et al., Experimental and numerical study of product gas and N_2O emission characteristics of ammonia/hydrogen/air premixed laminar flames stabilized in a stagnation flow. *Proceedings of the Combustion Institute,* 2022. **39**: pp. 1–9.
28. Jin, B.-Z., et al., Experimental and numerical study of the laminar burning velocity of NH_3/H_2/air premixed flames at elevated pressure and temperature. *International Journal of Hydrogen Energy*, 2022. **47**(85): pp. 36046–36057.
29. Berwal, P., and Kumar, S., Laminar burning velocity measurement of CH_4/H_2/NH_3-air premixed flames at high mixture temperatures. *Fuel*, 2023. **331**: p. 125809.
30. Chen, X., et al., Experimental and chemical kinetic study on the flame propagation characteristics of ammonia/hydrogen/air mixtures. *Fuel*, 2023. **334**: p. 126509.
31. Wang, Z., et al., Experimental and numerical study on laminar premixed NH_3/H_2/O_2/air flames. *International Journal of Hydrogen Energy*, 2023. **48**: pp. 14885–14895.
32. Zhou, S., et al., An experimental and kinetic modeling study on NH_3/air, NH_3/H_2/air, NH_3/CO/air, and NH_3/CH_4/air premixed laminar flames at elevated temperature. *Combustion and Flame*, 2023. **248**: p. 112536.
33. Zhang, X., et al., Combustion chemistry of ammonia/hydrogen mixtures: Jet-stirred reactor measurements and comprehensive kinetic modeling. *Combustion and Flame*, 2021. **234**: p. 111653.
34. Osipova, K.N., et al., Ammonia and ammonia/hydrogen blends oxidation in a jet-stirred reactor: Experimental and numerical study. *Fuel*, 2022. **310**: p. 122202.
35. Thorsen, L.S., et al., High pressure oxidation of NH_3/n-heptane mixtures. *Combustion and Flame*, 2023. **254**, p. 112785.
36. Dai, L., et al., Experimental and numerical analysis of the autoignition behavior of NH_3 and NH_3/H_2 mixtures at high pressure. *Combustion and Flame*, 2020. **215**: pp. 134–144.
37. Rocha, R.C., et al., Combustion of NH_3/CH_4/air and NH_3/H_2/air mixtures in a porous burner: Experiments and kinetic modeling. *Energy & Fuels*, 2019. **33**(12): pp. 12767–12780.
38. Puechberty, D. and M.J. Cottereau, Nitric oxide formation in an ammonia-doped methane-oxygen low pressure flame. *Combustion and Flame*, 1983. **51**: pp. 299–311.
39. Rosier, B., et al., Carbon monoxide concentrations and temperature measurements in a low pressure CH_4–O_2–NH_3 flame. *Applied Optics*, 1988. **27**(2): pp. 360–364.
40. Garo, A., C. Hilaire, and D. Puechberty, Experimental study of methane-oxygen flames doped with nitrogen oxide or ammonia. Comparison with modeling. *Combustion Science and Technology*, 1992. **86**(1–6): pp. 87–103.
41. Rahinov, I., A. Goldman, and S. Cheskis, Absorption spectroscopy diagnostics of amidogen in ammonia-doped methane/air flames. *Combustion and Flame*, 2006. **145**(1): pp. 105–116.

42. Tian, Z., et al., An experimental and kinetic modeling study of premixed $NH_3/CH_4/O_2$/Ar flames at low pressure. *Combustion and Flame*, 2009. **156**(7): pp. 1413–1426.
43. Li, B., et al., Measurements of NO concentration in NH_3-doped CH_{4+}air flames using saturated laser-induced fluorescence and probe sampling. *Combustion and Flame*, 2013. **160**(1): pp. 40–46.
44. Lamoureux, N., et al., Measurements and modelling of nitrogen species in $CH_4/O_2/N_2$ flames doped with NO, NH_3, or $NH_{3+NO.}$ *Combustion and Flame*, 2017. **176**: pp. 48–59.
45. Brackmann, C., et al., Formation of NO and NH in NH_3-doped $CH_4 + N_2 + O_2$ flame: Experiments and modelling. *Combustion and Flame*, 2018. **194**: pp. 278–284.
46. Ramos, C.F., et al., Experimental and kinetic modelling investigation on NO, CO and NH_3 emissions from NH_3/CH_4/air premixed flames. *Fuel*, 2019. **254**: pp. 115693.
47. Colson, S., et al., Experimental and numerical study of NH_3/CH_4 counterflow premixed and non-premixed flames for various NH_3 mixing ratios. *Combustion Science and Technology*, 2021. **193**(16): pp. 2872–2889.
48. Shi, H., et al., Experimental study and mechanism analysis of the NO_x emissions in the NH_3 MILD combustion by a novel burner. *Fuel*, 2022. **310**: p. 122417.
49. Montgomery, M.J., et al., Effect of ammonia addition on suppressing soot formation in methane co-flow diffusion flames. *Proceedings of the Combustion Institute,* 2021. **38**(2): pp. 2497–2505.
50. Bell, J.B., et al., Detailed modeling and laser-induced fluorescence imaging of nitric oxide in a NH_3-seeded non-premixed methane/air flame. *Proceedings of the Combustion Institute,* 2002. **29**(2): pp. 2195–2202.
51. Wang, Z., et al., Experimental and kinetic study on the laminar burning velocities of NH_3 mixing with CH_3OH and C_2H_5OH in premixed flames. *Combustion and Flame*, 2021. **229**: p. 111392.
52. Ronan, P., et al., Laminar flame speed of ethanol/ammonia blends: An experimental and kinetic study. *Fuel Communications*, 2022. **10**: p. 100052.
53. Li, M., et al., An experimental and modeling study on auto-ignition kinetics of ammonia/methanol mixtures at intermediate temperature and high pressure. *Combustion and Flame*, 2022. **242**: p. 112160.
54. Li, X., et al., Effect of methanol blending on the high-temperature auto-ignition of ammonia: An experimental and modeling study. *Fuel*, 2023. **339**, 126911: pp. 1–11.
55. Li, M., et al., Experimental and kinetic modeling study on auto-ignition properties of ammonia/ethanol blends at intermediate temperatures and high pressures. *Proceedings of the Combustion Institute,* 2022. **39**: pp. 1–9.
56. Xiao, H. and H. Li, Experimental and kinetic modeling study of the laminar burning velocity of NH_3/DME/air premixed flames. *Combustion and Flame*, 2022. **245**: pp. 112372.
57. Chen, J. and X. Gou, Experimental and kinetic study on the extinction characteristics of ammonia-dimethyl ether diffusion flame. *Fuel*, 2023. **334**: p. 126743.
58. Issayev, G., et al., Ignition delay time and laminar flame speed measurements of ammonia blended with dimethyl ether: A promising low carbon fuel blend. *Renewable Energy*, 2022. **181**: pp. 1353–1370.
59. Dai, L., et al., Ignition delay times of NH_3/DME blends at high pressure and low DME fraction: RCM experiments and simulations. *Combustion and Flame*, 2021. **227**: pp. 120–134.
60. Murakami, Y., et al., Effects of mixture composition on oxidation and reactivity of DME/NH_3/air mixtures examined by a micro flow reactor with a controlled temperature profile. *Combustion and Flame*, 2022. **238**: p. 111911.
61. Issayev, G., et al., Combustion behavior of ammonia blended with diethyl ether. *Proceedings of the Combustion Institute,* 2021. **38**(1): pp. 499–506.
62. Hashemi, H., et al., High-pressure oxidation of ethane. *Combustion and Flame*, 2017. **182**: pp. 150–166.
63. Hashemi, H., et al., High-pressure oxidation of propane. *Proceedings of the Combustion Institute,* 2019. **37**(1): pp. 461–468.
64. Payne, M.C., et al., Iterative minimization techniques for ab initio total-energy calculations: Molecular dynamics and conjugate gradients. *Reviews of Modern Physics*, 1992. **64**(4): p. 1045.
65. Zhao, H., et al., Studies of high-pressure n-butane oxidation with CO_2 dilution up to 100 atm using a supercritical-pressure jet-stirred reactor. *Proceedings of Combustion Insittute,* 2021. **38**: pp. 279–287.
66. Yan, C., et al., Low-and intermediate-temperature oxidation of dimethyl ether up to 100 atm in a supercritical pressure jet-stirred reactor. *Combustion and Flame*, 2022. **243**: p. 112059.
67. Wang, Z., et al., Study of low-and intermediate-temperature oxidation kinetics of diethyl ether in a supercritical pressure jet-stirred reactor. *The Journal of Physical Chemistry A*, 2023, **127**(2): pp. 506–516.
68. Klippenstein, S.J., et al., The role of NNH in NO formation and control. *Combustion and Flame*, 2011. **158**(4): pp. 774–789.

69. Klippenstein, S.J. and P. Glarborg, Theoretical kinetics predictions for NH_2+HO_2. *Combustion and Flame*, 2022. **236**: p. 111787.
70. Zhou, M., et al., Kinetic effects of NO addition on n-dodecane cool and warm diffusion flames. *Proceedings of the Combustion Institute,* 2021. **38**(2): pp. 2351–2360.
71. Glarborg, P., et al., On the rate constant for $NH_{2+}HO_2$ and third-body collision efficiencies for NH_2+H (+M) and NH_2+NH_2 (+M). *The Journal of Physical Chemistry A*, 2021. **125**(7): pp. 1505–1516.
72. Sarathy, S.M., et al., Alcohol combustion chemistry. *Progress in Energy and Combustion Science*, 2014. **44**: pp. 40–102.
73. Wang, Z., et al., Study on cool flame radical index and oxygen concentration dependence of oxygenated fuels. *Combustion and Flame*, 2023, **257**, 112493: pp. 1–7.
74. Wang, Z., et al., Kinetics and extinction of non-premixed cool and warm flames of dimethyl ether at elevated pressure. *Proceedings of Combustion Insittute,* 2022. **39**: pp. 1–8.
75. Wang, Y., et al., Ignition of dimethyl ether/air mixtures by hot particles: Impact of low temperature chemical reactions. *Proceedings of the Combustion Institute,* 2021. **38**: pp. 2459–2466 .
76. Felsmann, D., et al., Contributions to improving small ester combustion chemistry: Theory, model and experiments. *Proceedings of the Combustion Institute,* 2017. **36**(1): pp. 543–551.
77. Diévart, P., et al., A comparative study of the chemical kinetic characteristics of small methyl esters in diffusion flame extinction. *Proceedings of the Combustion Institute,* 2013. **34**(1): pp. 821–829.
78. Ju, Y., Understanding cool flames and warm flames. *Proceedings of the Combustion Institute,* 2021. **38**(1): pp. 83–119.
79. Ju, Y., et al., Dynamics of cool flames. *Progress in Energy and Combustion Science*, 2019. **75**(100787): p. 39.
80. Curran, H.J., et al., A comprehensive modeling study of n-heptane oxidation. *Combustion and Flame*, 1998. **114**(1–2): pp. 149–177.
81. Westbrook, C.K., et al., A detailed chemical kinetic reaction mechanism for n-alkane hydrocarbons from n-octane to n-hexadecane. *Combustion and Flame*, 2009. **156**(1): pp. 181–199.
82. Harper, M.R., et al., Comprehensive reaction mechanism for n-butanol pyrolysis and combustion. *Combustion and Flame*, 2011. **158**(1): pp. 16–41.
83. Herbinet, O., W.J. Pitz, and C.K. Westbrook, Detailed chemical kinetic mechanism for the oxidation of biodiesel fuels blend surrogate. *Combustion and Flame*, 2010. **157**(5): pp. 893–908.
84. Curran, H.J., Developing detailed chemical kinetic mechanisms for fuel combustion. *Proceedings of the Combustion Institute,* 2019. **37**(1): pp. 57–81.
85. Metcalfe, W.K., et al., A hierarchical and comparative kinetic modeling study of C1 − C2 hydrocarbon and oxygenated fuels. *International Journal of Chemical Kinetics*, 2013. **45**(10): pp. 638–675.
86. Yehia, O.R., C.B. Reuter, and Y. Ju, Low-temperature multistage warm diffusion flames. *Combustion and Flame*, 2018. **195**: pp. 63–74.
87. Yehia, O.R., C.B. Reuter, and Y. Ju, On the chemical characteristics and dynamics of n-alkane low-temperature multistage warm diffusion flames. *Proceedings of the Combustion Institute,* 2019. **37**(2): pp. 1717–1724.
88. Farouk, T., D. Dietrich, and F.L. Dryer, Three stage cool flame droplet burning behavior of n-alkane droplets at elevated pressure conditions: Hot, warm and cool flame. *Proceedings of the Combustion Institute,* 2019. **37**: pp. 3353–3361.
89. Skodje, R.T., et al., Theoretical validation of chemical kinetic mechanisms: Combustion of methanol. *The Journal of Physical Chemistry A*, 2010. **114**(32): pp. 8286–8301.
90. Ju, Y. and W. Sun, Plasma assisted combustion: Dynamics and chemistry. *Progress in Energy and Combustion Science*, 2015. **48**: pp. 21–83.
91. Zhong, H., et al., Kinetic studies of excited singlet oxygen atom O (1D) reactions with ethanol. *International Journal of Chemical Kinetics*, 2021. **53**(6): pp. 688–701.
92. Yan, C., et al., The kinetic study of excited singlet oxygen atom O(1D) reactions with acetylene. *Combustion and Flame*, 2020. **212**: pp. 135–141.
93. Ombrello, T., et al., Flame propagation enhancement by plasma excitation of oxygen. Part II: Effects of O_2 (a 1 Δ g). *Combustion and Flame*, 2010. **157**(10): pp. 1916–1928.
94. Ombrello, T., et al., Flame propagation enhancement by plasma excitation of oxygen. Part I: Effects of O_3. *Combustion and flame*, 2010. **157**(10): pp. 1906–1915.
95. Sepulveda, J., et al., Kinetic enhancement of microchannel detonation transition by ozone addition to acetylene mixtures. *AIAA Journal*, 2019. **57**(2): pp. 476–481.

96. Sun, W., et al., The effect of ozone addition on combustion: Kinetics and dynamics. *Progress in Energy and Combustion Science*, 2019. **73**: pp. 1–25.
97. Rousso, A.C., et al., Low-temperature oxidation of ethylene by ozone in a jet-stirred reactor. *The Journal of Physical Chemistry A*, 2018. **122**(43): pp. 8674–8685.
98. Mao, X., et al., Numerical modeling of ignition enhancement of CH_4/O_2/He mixtures using a hybrid repetitive nanosecond and DC discharge. *Proceedings of the Combustion Institute,* 2019. **37**: pp. 5545–5552.
99. Mao, X., et al., Effects of controlled non-equilibrium excitation on H_2/O_2/He ignition using a hybrid repetitive nanosecond and DC discharge. *Combustion and Flame*, 2019. **206**: pp. 522–535.
100. Alexander, S. and S. Alexander, Theoretical analysis of reaction kinetics with singlet oxygen molecules. *Physical Chemistry Chemical Physics (PCCP)*, 2011. **13**(36): pp. 16424–16436.
101. Sharipov, A.S. and A.M. Starik, Analysis of the reaction and quenching channels in a $H+O_2(a1\Delta g)$ system. *Physica Scripta*, 2013. **88**(5): p. 058305.
102. Chukalovsky, A.A., et al., Reaction of hydrogen atoms with singlet delta oxygen ($O_2(a1\Delta g)$). Is everything completely clear? *Journal of Physics D Applied Physics*, 2016. **49**(48): p. 485202.
103. Ju, Y., et al., Plasma assisted low temperature combustion. *Plasma Chemistry and Plasma Processing*, 2016. **36**(1): pp. 85–105.
104. Lefkowitz, J.K., et al., In situ species diagnostics and kinetic study of plasma activated ethylene dissociation and oxidation in a low temperature flow reactor. *Proceedings of the Combustion Institute,* 2015. **35**(3): pp. 3505–3512.
105. Lefkowitz, J.K., et al., Species and temperature measurements of methane oxidation in a nanosecond repetitively pulsed discharge. *Philosophical Transactions of the Royal Society A*, 2015. **373**(2048): p. 20140333.
106. Rousso, A., et al., Kinetic studies and mechanism development of plasma assisted pentane combustion. *Proceedings of the Combustion Institute,* 2019. **37**(4): pp. 5595–5603.
107. Rousso, A., et al., Low temperature oxidation and pyrolysis of n-heptane in nanosecond-pulsed plasma discharges. *Proceedings of the Combustion Institute,* 2017. **36**: pp. 4105–4112.
108. Zhong, H., et al., Kinetic studies of plasma assisted n-dodecane/O_2/N_2 pyrolysis and oxidation in a nanosecond-pulsed discharge. *Proceedings of Combustion Insittute,* 2021. **38**: pp. 6521–6531.
109. Zhong, H., et al. Kinetic studies of low-temperature ammonia oxidation in a nanosecond repetitively-pulsed discharge. In *AIAA SCITECH Forum, National Harbor*, Maryland, Jan. 23-27, 2023.
110. Kosarev, I.N., et al., Kinetics of ignition of saturated hydrocarbons by nonequilibrium plasma: CH_4-containing mixtures. *Combustion and Flame*, 2008. **154**(3): pp. 569–586.
111. Aleksandrov, N.L., et al., Mechanism of ignition by non-equilibrium plasma. *Proceedings of the Combustion Institute,* 2009. **32**(1): pp. 205–212.
112. Starikovskaya, S.M., et al., Ignition with low-temperature plasma: Kinetic mechanism and experimental verification. *High Energy Chemistry*, 2009. **43**(3): pp. 213–218.
113. Sun, W., et al., Kinetic effects of non-equilibrium plasma-assisted methane oxidation on diffusion flame extinction limits. *Combustion and Flame*, 2012. **159**(1): pp. 221–229.
114. Sun, W., et al., Direct ignition and S-curve transition by in situ nano-second pulsed discharge in methane/oxygen/helium counterflow flame. *Proceedings of the Combustion Institute,* 2013. **34**(1): pp. 847–855.
115. Lou, G., et al., Ignition of premixed hydrocarbon–air flows by repetitively pulsed, nanosecond pulse duration plasma. *Proceedings of the Combustion Institute,* 2007. **31**(2): pp. 3327–3334.
116. Uddi, M., et al., Nitric oxide density measurements in air and air/fuel nanosecond pulse discharges by laser induced fluorescence. *Journal of Physics D: Applied Physics*, 2009. **42**(7): p. 075205.
117. Uddi, M., et al., Atomic oxygen measurements in air and air/fuel nanosecond pulse discharges by two photon laser induced fluorescence. *Proceedings of the Combustion Institute,* 2009. **32**(1): pp. 929–936.
118. Yin, Z., et al., Measurements of temperature and hydroxyl radical generation/decay in lean fuel–air mixtures excited by a repetitively pulsed nanosecond discharge. *Combustion and Flame*, 2013. **160**(9): pp. 1594–1608.
119. Suib, S.L. and R.P. Zerger, A direct, continuous, low-power catalytic conversion of methane to higher hydrocarbons via microwave plasmas. *Journal of Catalysis*, 1993. **139**: pp. 381–391.
120. Lesueur, H., A. Czernichowski, and J. Chapelle, Electrically assisted partial oxidation of methane. *International Journal of Hydrogen Energy*, 1994. **19**(2): pp. 139–144.
121. Okumoto, M., et al., Nonthermal plasma approach in direct methanol synthesis from CH_4. *IEEE Transactions on Industry Applications*, 1998. **34**(5): pp. 940–944.
122. Bromberga, L., et al., Plasma catalytic reforming of methane. *International Journal of Hydrogen Energy*, 1999. **24**: pp. 1131–1137.

123. Lee, D.H., et al., Optimization scheme of a rotating gliding arc reactor for partial oxidation of methane. *Proceedings of the Combustion Institute,* 2007. **31**(2): pp. 3343–3351.
124. Hwang, N., Y.-H. Song, and M.S. Cha, Efficient use of CO_2 reforming of methane with an arc-jet plasma. *IEEE Transactions on Plasma Science*, 2010. **38**(12): pp. 3291–3299.
125. Zhang, X. and M.S. Cha, Electron-induced dry reforming of methane in a temperature-controlled dielectric barrier discharge reactor. *Journal of Physics D: Applied Physics*, 2013. **46**(41): p. 415205.
126. Zhang, X. and M.S. Cha, Partial oxidation of methane in a temperature-controlled dielectric barrier discharge reactor. *Proceedings of the Combustion Institute,* 2015. **35**: pp. 3447–3454.
127. Jasiński, M., M. Dors, and J. Mizeraczyk, Production of hydrogen via methane reforming using atmospheric pressure microwave plasma. *Journal of Power Sources*, 2008. **181**(1): pp. 41–45.
128. Sun, W., et al., Effects of non-equilibrium plasma discharge on counterflow diffusion flame extinction. *Proceedings of the Combustion Institute,* 2011. **33**(2): pp. 3211–3218.
129. Wang, H., et al., USC mech version II. High-temperature combustion reaction model of H_2/CO/C1-C4 compounds, 2007.
130. MacFarlane, D.R., et al., A roadmap to the ammonia economy. *Joule*, 2020. **4**(6): pp. 1186–1205.
131. Valera-Medina, A., et al., Ammonia for power. *Progress in Energy and Combustion Science*, 2018. **69**: pp. 63–102.
132. Afif, A., et al., Ammonia-fed fuel cells: A comprehensive review. *Renewable and Sustainable Energy Reviews*, 2016. **60**: pp. 822–835.
133. Pai, S.J., C.L. Heald, and J.G. Murphy, Exploring the global importance of atmospheric ammonia oxidation. *ACS Earth and Space Chemistry*, 2021. **5**(7): pp. 1674–1685.
134. Tang, Y., et al., Flammability enhancement of swirling ammonia/air combustion using AC powered gliding arc discharges. *Fuel*, 2022. **313**: p. 122674.
135. Choe, J., et al., Plasma assisted ammonia combustion: Simultaneous NO_x reduction and flame enhancement. *Combustion and Flame*, 2021. **228**: pp. 430–432.
136. Kim, G.T., et al., Effects of non-thermal plasma on turbulent premixed flames of ammonia/air in a swirl combustor. *Fuel*, 2022. **323**: p. 124227.
137. Zhong, H., et al., Understanding non-equilibrium N_2O/NO_x chemistry in plasma-assisted low-temperature NH_3 oxidation. *Combustion and Flame*, 2023. **256**: p. 112948.
138. Pancheshnyi, S., et al., The LXCat project: Electron scattering cross sections and swarm parameters for low temperature plasma modeling. *Chemical Physics*, 2012. **398**: pp. 148–153.
139. Zhao, H., X. Yang, and Y. Ju, Kinetic studies of ozone assisted low temperature oxidation of dimethyl ether in a flow reactor using molecular-beam mass spectrometry. *Combustion and Flame*, 2016. **173**: pp. 187–194.
140. Zhong, H., et al., Kinetic study of reaction $C_2H_5+HO_2$ in a photolysis reactor with time-resolved Faraday rotation spectroscopy. *Proceedings of the Combustion Institute,* 2021. **38**: pp. 871–880.
141. Teng, C.C., et al., Time-resolved HO_2 detection with Faraday rotation spectroscopy in a photolysis reactor. *Optics Express*, 2021. **29**(2): pp. 2769–2779.
142. Kee, R. J., Grear, J. F., Smooke, M. D. & Miller, J. A. 1985 Sandia Rep. SAND85-8240.
143. Cai, L., et al., Optimized reaction mechanism rate rules for ignition of normal alkanes. *Combustion and Flame*, 2016. **173**: pp. 468–482.
144. Zhao, H., et al., Studies of low temperature oxidation of n-pentane with nitric oxide addition in a jet stirred reactor. *Combustion and Flame*, 2018. **197**: pp. 78–87.
145. Lin, J., et al., Multiple dynamical pathways in the O (1 D)+ CH_4 reaction: A comprehensive crossed beam study. *The Journal of Chemical Physics*, 2000. **113**(13): pp. 5287–5301.
146. Yu, H.G. and J.T. Muckerman, MRCI calculations of the lowest potential energy surface for CH_3OH and direct ab initio dynamics simulations of the O (1D)+ CH_4 reaction. *The Journal of Physical Chemistry A*, 2004. **108**(41): pp. 8615–8623.
147. Luntz, A., Chemical dynamics of the reactions of O (1 D 2) with saturated hydrocarbons. *The Journal of Chemical Physics*, 1980. **73**(3): pp. 1143–1152.
148. Brumfield, B., et al., Dual modulation Faraday rotation spectroscopy of HO 2 in a flow reactor. *Optics Letters*, 2014. **39**(7): pp. 1783–1786.
149. Huang, C.-K., et al., Dynamics of the reactions of O (1D) with CD_3OH and CH_3OD studied with time-resolved Fourier-transform IR spectroscopy. *The Journal of Chemical Physics*, 2012. **137**(16): p. 164307.
150. Zhong, H., et al., Direct kinetic measurements and theoretical predictions of singlet oxygen atom reaction with dimethyl ether. *The Journal of Physical Chemistry Letters*, 2024. **15**, pp. 6158–6165.

151. Zhong, H., et al., Plasma thermal-chemical instability of low-temperature dimethyl ether oxidation in a nanosecond-pulsed dielectric barrier discharge. *Plasma Sources Science and Technology*, 2022. **31**(11): p. 114003.
152. Am Ano, T. and F.L. Dryer. Effect of dimethyl ether, NOx, and ethane on CH_4 oxidation: High pressure, intermediate-temperature experiments and modeling. in *Symposium (International) on Combustion*, 1998. Elsevier.
153. Zhao, H., et al., Experimental and modeling study of the mutual oxidation of n-pentane and nitrogen dioxide at low and high temperatures in a jet stirred reactor. *Energy*, 2018. **165**: pp. 727–738.
154. Eliasson, B., M. Hirth, and U. Kogelschatz, Ozone synthesis from oxygen in dielectric barrier discharges. *Journal of Physics D: Applied Physics*, 1987. **20**(11): p. 1421.
155. Johnston, H.S., Atmospheric ozone. *Annual Review of Physical Chemistry*, 1992. **43**(1): pp. 1–31.
156. Sandri, R., On the decomposition flame of liquid ozone-oxygen mixtures in a tube. *Combustion and Flame*, 1958. **2**(4): pp. 348–352.
157. Hajilou, M., et al., Experimental and numerical characterization of freely propagating ozone-activated dimethyl ether cool flames. *Combustion and Flame*, 2017. **176**: pp. 326–333.
158. Won, S.H., et al., Self-sustaining n-heptane cool diffusion flames activated by ozone. *Proceedings of the Combustion Institute,* 2015. **35**(1): pp. 881–888.
159. Halter, F., P. Higelin, and P. Dagaut, Experimental and detailed kinetic modeling study of the effect of ozone on the combustion of methane. *Energy & Fuels*, 2011. **25**(7): pp. 2909–2916.
160. Hippler, H., R. Rahn, and J. Troe, Temperature and pressure dependence of ozone formation rates in the range 1–1000 bar and 90–370 K. *The Journal of Chemical Physics*, 1990. **93**(9): pp. 6560–6569.
161. Patrick, R. and D.M. Golden, Kinetics of the reactions of amidogen radicals with ozone and molecular oxygen. *The Journal of Physical Chemistry*, 1984. **88**(3): pp. 491–495.
162. Masurier, J.-B., et al., Ozone applied to the homogeneous charge compression ignition engine to control alcohol fuels combustion. *Applied Energy*, 2015. **160**: pp. 566–580.
163. Tachibana, T., et al., Effect of ozone on combustion of compression ignition engines. *Combustion and Flame*, 1991. **85**(3–4): pp. 515–519.
164. Chen, C., et al., Experimental and kinetic modeling study of laminar burning velocity enhancement by ozone additive in $NH_{3+O2+N2}$ and $NH_{3+CH4}/C_2H_6/C_3H_{8+air\ flames.}$ *Proceedings of the Combustion Institute*, 2023. **39**: pp. 4237–4246.
165. Crane, J., et al., Isolating the effect of induction length on detonation structure: Hydrogen–oxygen detonation promoted by ozone. *Combustion and Flame*, 2019. **200**: pp. 44–52.
166. Alfazazi, A., et al., Cool diffusion flames of butane isomers activated by ozone in the counterflow. *Combustion and Flame*, 2018. **191**: pp. 175–186.
167. Alam, F.E., et al., Ozone assisted cool flame combustion of sub-millimeter sized n-alkane droplets at atmospheric and higher pressure. *Combustion and Flame*, 2018. **195**: pp. 220–231.
168. Warnatz, J., Calculation of the structure of laminar flat flames I: Flame velocity of freely propagating ozone decomposition flames. *Berichte der Bunsengesellschaft für physikalische Chemie*, 1978. **82**(2): pp. 193–200.
169. Lee, M., et al., Experimental observation and numerical simulation of wall-stabilized premixed cool flames. *Proceedings of the Combustion Institute,* 2019. **37**: pp. 1749–1756.
170. Reuter, C.B., et al., Study of the low-temperature reactivity of large n-alkanes through cool diffusion flame extinction. *Combustion and Flame*, 2017. **179**: pp. 23–32.
171. Reuter, C.B., S.H. Won, and Y. Ju, Experimental study of the dynamics and structure of self-sustaining premixed cool flames using a counterflow burner. *Combustion and Flame*, 2016. **166**: pp. 125–132.
172. Won, S.H., et al., A new cool flame: Establishment and studies of dynamics and kinetics. *52nd Aerospace Sciences Meeting,* (doi: 10.2514/6.2014-0818), in AIAA paper-2014-0818, 2014.
173. Foucher, F., et al., Influence of ozone on the combustion of n-heptane in a HCCI engine. *Proceedings of the Combustion Institute,* 2013. **34**(2): pp. 3005–3012.
174. Rousso, A.C., et al., Identification of the Criegee intermediate reaction network in ethylene ozonolysis: Impact on energy conversion strategies and atmospheric chemistry. *Physical Chemistry Chemical Physics*, 2019. **21**(14): pp. 7341–7357.
175. Rousso, A.C., et al., Extreme low-temperature combustion chemistry: Ozone-initiated oxidation of methyl hexanoate. *The Journal of Physical Chemistry A*, 2020. **124**(48): pp. 9897–9914.
176. Wu, B., et al., Dynamics of laminar ethylene lifted flame with ozone addition. *Proceedings of the Combustion Institute,* 2021. **38**(4): pp. 6773–6780.

177. Gutbrod, R., et al., Formation of OH radicals in the gas phase ozonolysis of alkenes: The unexpected role of carbonyl oxides. *Chemical Physics Letters*, 1996. **252**(3–4): pp. 221–229.
178. Osborn, D.L. and C.A. Taatjes, The physical chemistry of Criegee intermediates in the gas phase. *International Reviews in Physical Chemistry*, 2015. **34**(3): pp. 309–360.
179. Taatjes, C.A., et al., Direct observation of the gas-phase Criegee intermediate (CH_2OO). *Journal of the American Chemical Society*, 2008. **130**(36): pp. 11883–11885.
180. Anglada, J.M., R. Crehuet, and J.M. Bofill, The ozonolysis of ethylene: A theoretical study of the gas-phase reaction mechanism. *Chemistry: A European Journal*, 1999. **5**(6): pp. 1809–1822.
181. Criegee, R., Mechanism of ozonolysis. *Angewandte Chemie International Edition in English*, 1975. **14**(11): pp. 745–752.